Conformational Landscapes of a Class I Ribonucleotide Reductase Complex during Turnover Reveal Intrinsic Dynamics and Asymmetry

Da Xu[1], William C. Thomas[1,2], Audrey A. Burnim[1], and Nozomi Ando[1,2†]

[1]Department of Chemistry and Chemical Biology, Cornell University, Ithaca, NY 14853, USA.
[2]Department of Chemistry, Princeton University, Princeton, NJ, 08544, USA.

[†] Correspondence should be addressed to nozomi.ando@cornell.edu.

Abstract: Understanding the structural dynamics associated with enzymatic catalysis has been a long-standing goal of structural biology. A wide range of motions, from small side-chain fluctuations to large domain rearrangements, have been implicated in enzyme function by experimental and computational studies. However, because structural techniques generally depend on averaging, direct visualization of conformational landscapes during turnover has been challenging. Here, we report the conformational landscapes of a class I ribonucleotide reductase (RNR) in various stages of turnover using single-particle cryo-electron microscopy (cryo-EM) and a combination of classification and deep-learning-based analyses. RNRs are responsible for the conversion of ribonucleotides to deoxyribonucleotides, a reaction that is essential for all DNA-based life. Class I RNRs, used by humans and other aerobic organisms, perform a complex series of chemical steps that are coupled with the dynamics of two highly mobile subunits, which can be resolved by EM. We demonstrate that despite the dimeric nature of the enzyme and its intrinsic dynamics, remarkable asymmetry is maintained across the class I RNR complex that physically segregates the two halves of its turnover cycle.

Main Text

Ribonucleotide reductases (RNRs) are essential enzymes in all free-living organisms, as they enable the only *de novo* synthesis pathway of 2′-deoxyribonucleotides, the building blocks for DNA (*1*). Despite wide evolutionary diversity (*2*, *3*), all RNRs share a common catalytic mechanism initiated by the formation of a thiyl radical on a conserved active-site cysteine (*4*). The oxygen-dependent class I RNRs (*5*, *6*) are used by aerobic life, including most eukaryotes, many prokaryotes, and associated viruses (*2*, *3*). These RNRs have long fascinated researchers for their relevance as drug targets and for their dynamic quaternary structure involving two subunits (Figure 1A): 1) a small ferritin-like subunit (β) that houses a stable radical cofactor, and 2) a large catalytic subunit (α) that contains the nucleotide-binding sites, including the active site, an allosteric site that controls substrate specificity, and additional allosteric sites involved in regulating overall enzyme activity.

Decades of research, especially on the *Escherichia coli* (*Ec*) class Ia RNR, have delineated the turnover cycle of class I RNRs (*1*, *7*), which consists of two halves: catalysis and re-reduction (Figure 1B). The catalysis half-cycle begins with proton-coupled electron transfer (PCET) along a series of amino acids that transfers the radical from the cofactor in the β subunit to the catalytic cysteine in the α subunit. Radical transfer initiates reduction of the substrate and concomitant oxidation of an additional pair of active-site cysteines. The radical then transfers back to the β subunit to complete the cycle. In the re-reduction half-cycle, the oxidized active-site cysteines are reduced by a cysteine pair located on the flexible α C-terminal tail, which is in turn reduced by external reductants, such as thioredoxins, resetting the enzyme for a new round of catalysis. For PCET to occur, the class I subunits interact as dimers (α_2 and β_2) to form an active $\alpha_2\beta_2$ complex (Figure 1A), but this complex has proven to be highly dynamic, posing a major challenge for high-resolution structural characterization. Recently, the first structure of an active class I RNR complex was reported by cryo-electron microscopy (cryo-EM) using unnatural amino acid incorporation to trap the enzyme in a PCET-competent conformation (*8*). This landmark study revealed striking asymmetry within the *Ec* class Ia RNR complex, with α and β closely engaged on one side and the flexible β C-terminus folded into the active site to contribute an interfacial PCET residue, thereby providing a structural basis for

multiple lines of evidence that suggest half-site reactivity (*9–17*). Despite these remarkable advances, the full set of conformations needed for enzymatic turnover have remained enigmatic. Moreover, direct links cannot be made between discrete structural states and enzyme kinetics.

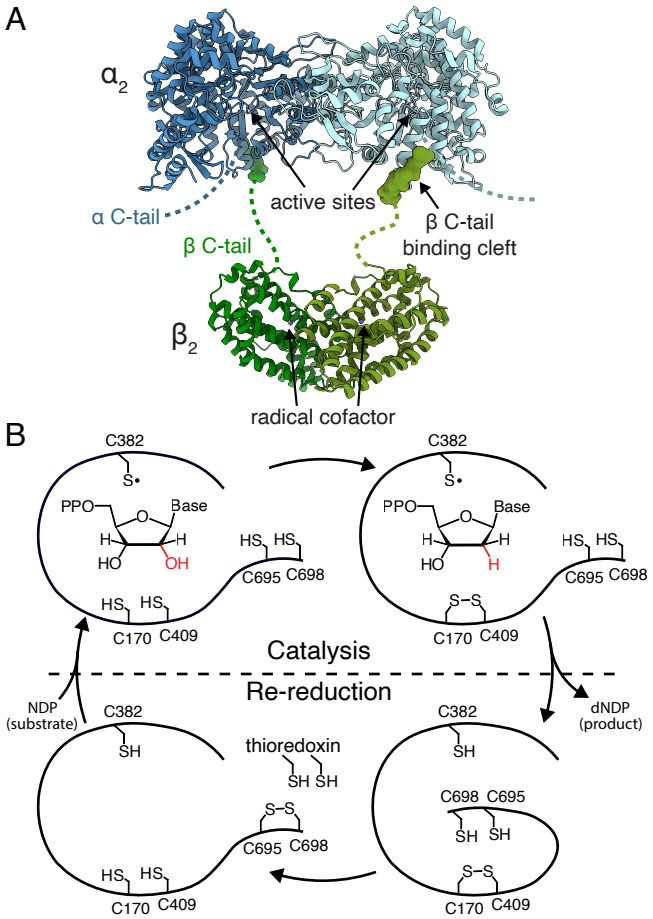

Figure 1. Class I ribonucleotide reductases (RNRs) require dynamic components for turnover. (A) The α_2 subunit in *Bacillus subtilis* (*Bs*) class Ib RNR (pdb: 6mt9, blue) houses the active site and allosteric sites (*18*). The β_2 subunit (pdb: 4dr0, green) houses a dimanganese tyrosyl radical cofactor (*19*). Both subunits are homodimeric and have functionally essential C-terminal tails, which are flexible (dashed). The two subunits are stably tethered through a strong interaction between the β C-terminus and its binding cleft on the α subunit (pdb: 6mw3, surface), but the interaction between the core parts of α_2 and β_2 is very dynamic. (B) The turnover cycle of class I RNRs with *Bs* numbering. PCET between the two subunits generates a thiyl radical (C382•) in the active site, which initiates reduction of ribonucleoside diphosphates to 2′-deoxyribonucleoside diphosphates. Active-site cysteines (C170/C409), which are oxidized during substrate reduction, are reduced by cysteines on the α C-terminal tail (C695/C698), which are in turn reduced by external reductants such as thioredoxins.

Here, we used cryo-EM to investigate the conformational landscapes of the class I RNR from *Bacillus subtilis* (*Bs*) during turnover. *Bs* RNR employs a class Ib cofactor (a dimanganese tyrosyl radical) to achieve activities comparable to *Ec* class Ia RNR (*20*). Moreover, *Bs* RNR exhibits attractive features for the study of structural dynamics. Namely, the α/β interactions have a K_m of 25 nM (*20*), implying a substantially stronger affinity than that reflected by the K_d of 0.2 μM for *Ec* RNR (*21*). Additionally, we had previously shown by small-angle X-ray scattering (SAXS) that the enzyme forms a nearly homogenous solution of $\alpha_2\beta_2$ tetramers when provided with substrate guanosine diphosphate (GDP), specificity effector thymidine

triphosphate (TTP), and activator adenosine triphosphate (ATP) (*18*). Cryo-EM also revealed that with allosteric inhibitors, the $\alpha_2\beta_2$ complexes assemble into long filaments that confine the motions of β_2 relative to α_2 (*18*), suggesting that class I RNRs require significant motions to sustain turnover.

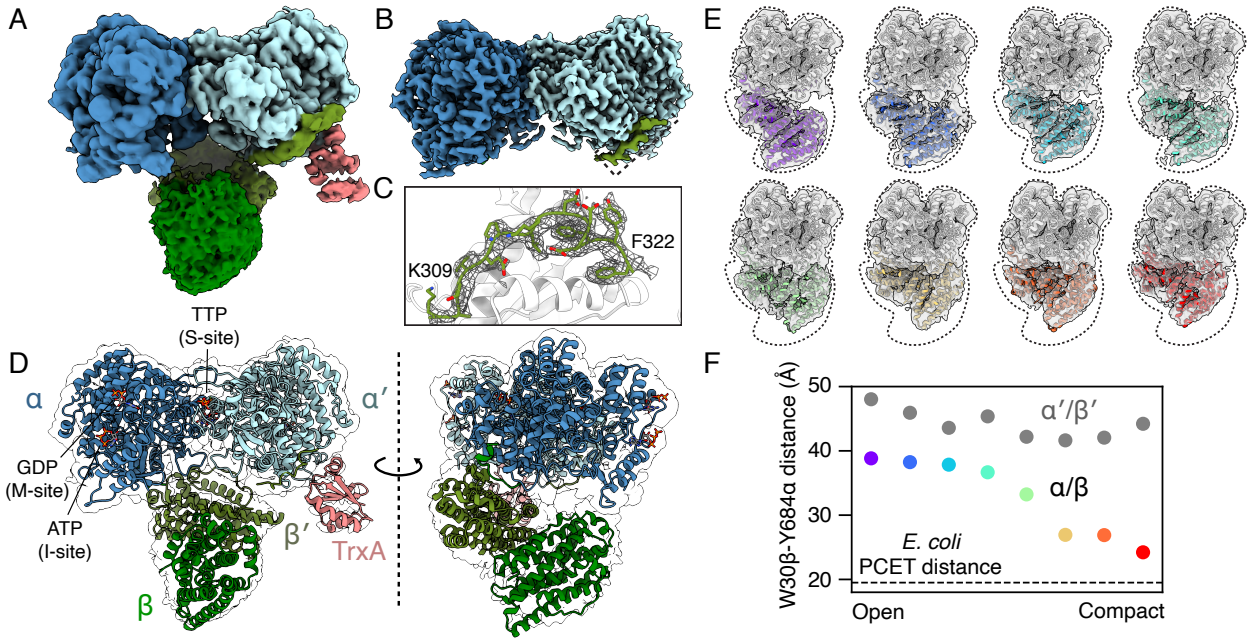

Figure 2. Cryo-EM reconstructions of *Bs* RNR during active turnover reveal continuous motions that maintain functional asymmetry. (A) Unsharpened consensus map contains density for α_2 (blue) and β_2 (green), as well as additional density on one side of α_2 corresponding to TrxA (coral). (B) Sharpened consensus map contains high-resolution information for α_2 and residues 309-322 of the β C-termini (green surface in dashed box). (C) The bound β C-terminus (mesh) is well-resolved on both sides of α_2. (D) Consensus model of the *Bs* RNR complex produced by docking a refined model of α_2 with the β C-terminus and allosteric effectors (ATP, TTP, GDP) bound to each monomer and the atomic models of β_2 and TrxA into the unsharpened map (Methods). Surprising asymmetry is observed in β_2 and TrxA binding. (E) 3D classification reveals continuous motion of β_2 from open to compact (left to right, top to bottom), shown in same side-view orientation as in panel D. (F) Asymmetry is observed across all 3D classes, as shown by distance between interfacial residues involved in PCET: W30β and Y684α. Only one side of the RNR complex (α/β pair) can approach the proximity needed for PCET, while the other side (α′/β′ pair) remains separated by a long distance. Colors of individual points are consistent with panel E.

To characterize these motions, we examined a cryo-EM dataset collected on a sample flash-frozen within 20 s of initiating turnover in *Bs* RNR in the presence of GDP, TTP, ATP, and its endogenous reducing system, thioredoxin (TrxA) and NADPH-dependent thioredoxin reductase (TrxB) (Methods). In the resulting 3D consensus reconstruction (Figure 2A-B, Table S1), particles are aligned on α_2 (160 kDa) to ~2.5-Å resolution, while the smaller β_2 (80 kDa) is blurred. However, we observe high-resolution density for the β C-terminus (K309 – F322) bound on both sides of α_2 (Figure 2B-C), indicating that the blurring is not caused by low β occupancy, but rather by a dynamic β_2 subunit that is tethered to α_2 via its C-terminal tails (Figure 1A). Although low resolution, the β_2 density in the consensus map is consistent with its crystal structure (*19*). A consensus model of the full complex was therefore built by refining an atomic model of α_2 bound with nucleotides and β C-termini and docking the β_2 crystal structure (Figure 2D). Reminiscent of the *Ec* RNR structure (*8*), we observe β_2 asymmetrically bound to α_2 but more open and not as closely engaged. As a result, the monomers within α_2 and β_2 are no longer identical, and we can associate each β subunit with the α subunit where its tail binds to define two pairs: α/β and α′/β′ (Figure 2D). Focused 3D classification of β_2 resulted in discrete classes that reveal a wide range of $\alpha_2\beta_2$ conformations, from open to

compact (Figure 2E, Table S2). The β_2 density in these classes exhibits clear secondary structural details that fit the docked crystal structure, supporting the interpretation that the blurring in the consensus map is due to motion. Interestingly, we do not observe 3D classes that match the PCET conformation seen in *Ec* RNR, likely indicating its low prevalence in this highly heterogeneous conformational ensemble.

In addition to asymmetrically bound β_2, we observed a small feature in the consensus map on only one side of α_2 (Figure 2A). Upon examining the remaining protein components in the reaction mixture, we found that an atomic model of TrxA fits unambiguously into the density (Figures 2D, S1A), representing the first visualization of a thioredoxin-RNR interaction. Like the β_2 density, TrxA density disappears with sharpening, in this case owing to lower occupancy, as will be detailed later. Nonetheless, the asymmetric binding of β_2 and TrxA has profound implications for the half-site reactivity of the class I RNR mechanism. PCET requires interfacial residues between α_2 and β_2 (W30β → Y307β → Y684α) to come in proximity (*1*). Whereas Y307β is on the unresolved region (residues 291-308) of the β C-terminal tail, it is two residues away from the tail segment that is bound to α_2, near the opening of the active site, and therefore must not be far from Y684α (Figure S2A). However, the asymmetric posing of β_2 relative to α_2 causes large differences in the separation between W30β and Y684α on the two sides of the complex. We see that W30β-Y684α distances on one side (α/β) can approach the distance needed for the disordered region of the β C-terminus to fold into the active site for PCET (Figure 2F). In contrast, distances on the other side (α′/β′) are too long for PCET, consistent with the fact that in certain 3D classes, the density for the β C-terminal tail appears stretched across this gap (Figure S2B). Interestingly, TrxA, which is required for re-reduction, preferentially binds to the α′/β′ side where PCET cannot occur. This asymmetry suggests that the enzyme has evolved a mechanism for segregating catalysis and re-reduction processes across its two halves.

To understand how the conformational ensemble is coupled to the turnover process, we collected three additional cryo-EM datasets with slight alterations to the reaction mixture (Table S1): a pre-turnover condition (lacking substrate), a product condition (replacing substrate with product), and a pre-reduction condition (stalled re-reduction due to depletion of NADPH after multiple turnovers). For all three datasets, we obtained 3D consensus reconstructions showing similarly blurry β_2 but with varying TrxA occupancy (Figure S3, Tables S1-S2). Consistent with the expectation that the enzyme remains reduced in the pre-turnover and product conditions (due to lack of turnover), density for the active-site C170/C409 pair appears largely reduced, while they are largely oxidized in the pre-reduction condition and a mixture of reduced and oxidized in the turnover condition (Figure S4).

Interestingly, TrxA occupancy in the consensus maps appears to be correlated with the level of active-site oxidation, with the pre-reduction condition exhibiting the strongest density, followed by the turnover condition, and the two non-turnover conditions (pre-turnover, product) having similarly low occupancies (Figure S3). 3D classification of β_2 in each condition yielded 3-8 classes that resemble the open and compact conformations seen in the turnover condition, suggesting that there are intrinsic conformational dynamics that are shared even in the absence of turnover (Figure S6A-D, Table S2). Remarkably, 3D classification of a refinement of particles combined from all conditions (Figure S6E, Table S2) resolved a new conformation, which closely resembles the PCET conformation seen in *Ec* RNR (Figure S7A-B). However, no density for the β C-terminus is observed in the active site in this class (Figure S7C), indicating that this conformation, while PCET-like in the relative α_2/β_2 positioning, does not exactly correspond to the PCET process and that the PCET conformation is highly transient.

Because 3D classes appeared to represent a continuum of motions, we employed a deep-learning method, cryoDRGN (*22*, *23*), to obtain conformational landscapes. Briefly, a cryoDRGN model was trained for each condition, after which 1000 volumes were generated from the latent space based on particle clustering (Methods). Atomic models of α_2 and β_2 were rigid-body fit into each volume, and the relative orientation of β_2 from α_2 was parametrized as a 7D coordinate representing the transformation (translation/rotation) between two coordinate systems defined on α_2 and β_2 individually. The 7D coordinates from all conditions

were combined and embedded in 2D using DensMAP (density-preserving manifold approximation and projection (*24*)), from which a probability distribution was estimated to represent the combined conformational landscape of β_2 orientations (Figure 3A). The joint embeddings of β_2 orientations were then separated by condition to produce individual landscapes (Figure 3B-E). We note that due to the particle filtering involved in the cryoDRGN training process and finite sampling of the latent space, low-population conformations may not be observed. However, processing was kept consistent between conditions such that comparisons can be made confidently. Importantly, discrete 3D classes fit well within these representations and showed consistency between conventional classification and deep-learning based analyses (Figure S8, Table S3). By mapping the resulting landscapes with metrics that describe the openness of β_2 with respect to α_2 (Figure S9A-B) and by mapping the coordinates of representative 3D classes (Figure 3A), we find that a trajectory from left to right correlates with a continuous transition from open to compact conformations, while the bottom-right quadrant contains PCET-like conformations. Notably, symmetric β_2 orientations are essentially not observed (Figure S9C), and thus, the landscapes represent a continuum of *asymmetric* open and compact $\alpha_2\beta_2$ conformations.

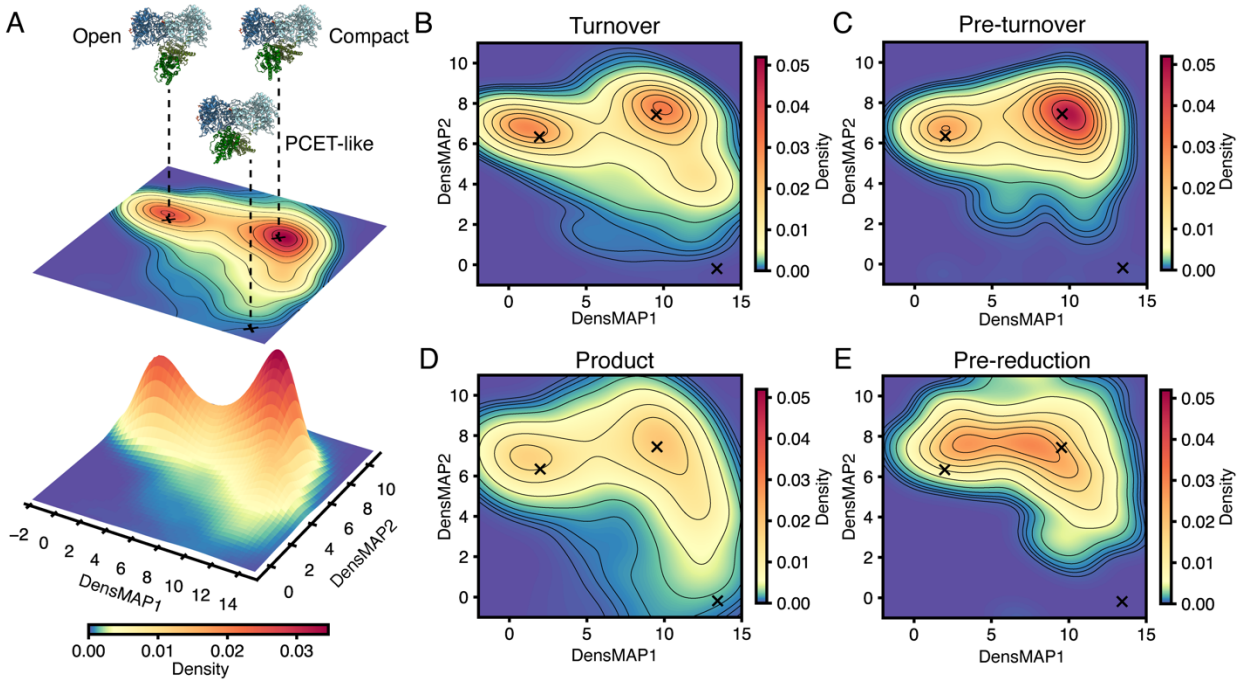

Figure 3. Conformational landscapes of *Bs* class Ib RNR highlight intrinsic dynamics and functionally relevant motions. Here, 7D coordinates representing the transformation (translation and rotation) between the α_2 and β_2 subunits are projected to 2D in a density-preserving representation (DensMAP), while the colorbar indicates population density (blue to red: low to high). (A) Joint conformational landscape obtained by combining coordinates from all conditions shown in panels B-E. Symmetric $\alpha_2\beta_2$ conformations are essentially not observed (Figure S9C). Locations of three 3D classes from the combined particle set are marked to aid interpretation: open, compact, and PCET-like correspond to classes 6, 23, and 15 in Figures S6E and S8A, all of which are asymmetric. (B-E) Conformational landscapes of individual conditions marked with the same three 3D classes as panel A. The enzyme exhibits intrinsic dynamics even before substrate is added (pre-turnover), while addition of substrate (turnover) or substrate analog (product) leads to an increased population of PCET-like conformations. A balance of open and compact populations is observed for the oxidized enzyme (pre-reduction), likely as a result of TrxA interactions.

The conformational landscapes from the individual conditions, while similar, are distinct from each other, indicating that RNR dynamics change throughout turnover (Figure 3B-E). Using the three marked coordinates corresponding to open, compact, and PCET-like conformations as visual guides, we see that in

the pre-turnover condition, compact conformations are enriched, although the enzyme samples many conformations. Interestingly, the turnover and product landscapes share similar topologies, while the latter is spread more towards PCET-like conformations. Comparing these landscapes highlights the intrinsic and continuous motions of RNR, which exist even before the substrate is introduced, while addition of substrate leads to the population of PCET-like conformations. Prior kinetics studies have shown that the rate of product formation during the catalysis half-cycle of class I RNRs is low (~5-10 s^{-1}) due to a slow step that precedes PCET and catalysis, which are orders of magnitude faster (>150 s^{-1}) (*7*, *20*, *25*). This step has long been proposed to be conformational in nature as it strongly correlates with the addition of substrate (*17*). Here, our landscapes show for the first time that substrate addition directly leads to a change in the conformational populations, such that a highly transient PCET conformation becomes accessible. Interestingly, we observe the largest population of PCET-like conformations in the product condition, suggesting that the product acts like a substrate analog when the enzyme is reduced. The PCET conformation may also be essential in the product-bound state to enable reverse radical transfer from the active site to the cofactor in the β subunit. In contrast, the pre-reduction condition exhibits more limited motion, and we observe an enrichment of open conformations, potentially due to increased TrxA interactions.

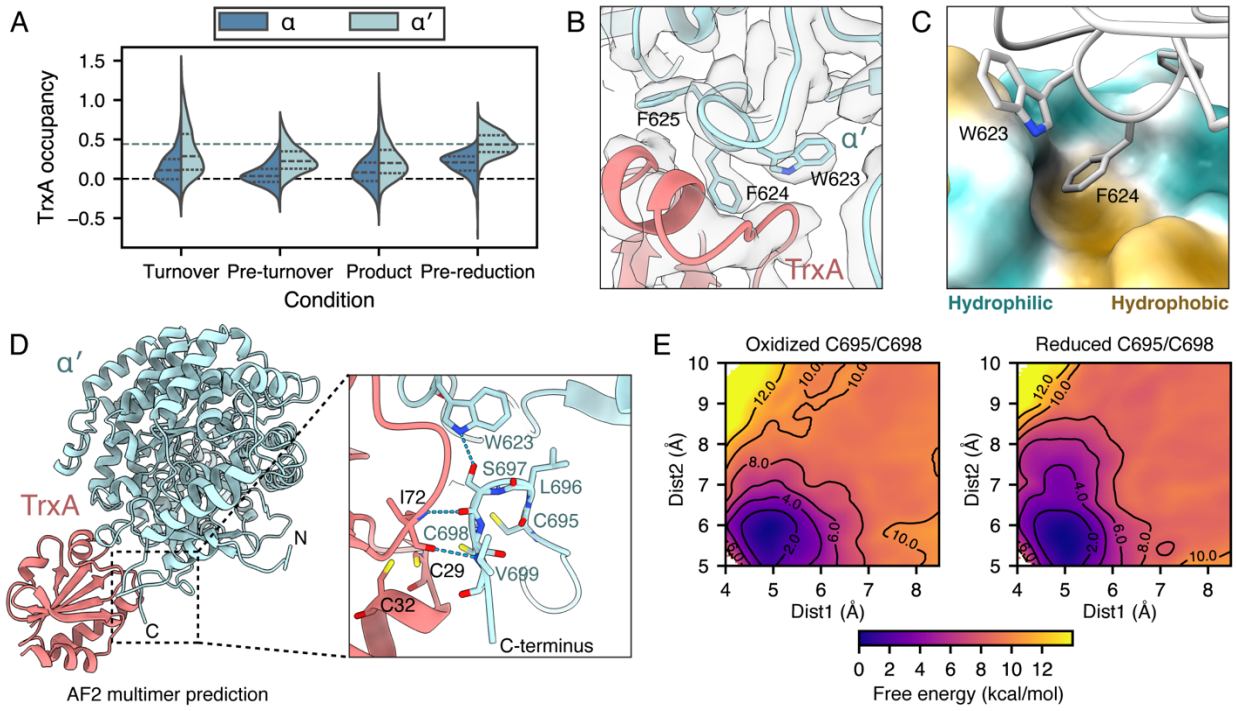

Figure 4. RNR-thioredoxin interactions favor the α′ side and depend on the oxidation state of α C-terminus. (A) Violin plot of TrxA occupancy obtained from landscape analysis, shown by condition and α_2 protomer with quartiles within each distribution marked by dashed lines. The highest TrxA occupancy is observed in the pre-reduction condition, while the largest variance is observed in the turnover condition, suggesting that TrxA preferentially binds oxidized RNR on the α′ side. (B) The interface between TrxA and the α′ subunit contains consecutive aromatic residues. Map shown is refined from particles with high TrxA occupancy from focused classification of pre-reduction dataset (Figure S1B). (C) F624α′ embeds in a hydrophobic pocket of TrxA, which is shown as surface colored by hydrophobicity. (D) AlphaFold2 multimer predictions of the TrxA-α′ complex depict the α′ C-terminal tail in a TrxA-bound conformation. (E) MD-generated 2D free energy landscapes of α′ C-terminal tail dissociation from TrxA-bound conformation show a steeper gradient when the C-terminal cysteine pair C695/C698 is oxidized, due to the rigidity provided by the disulfide bond. Two sampled distances are defined between the α′ C-terminal tail and its binding interface (Figure S12).

To investigate the molecular mechanisms of TrxA binding, we first estimated TrxA occupancy based on its map intensity relative to that of α_2 within individual volumes from cryoDRGN landscape analysis (Methods). Consistent with consensus reconstructions, we find that TrxA occupancy increases with α_2 oxidation (Figures 4A), with the largest variance in occupancy observed in the turnover condition, which is the most heterogeneous in oxidation state. We also find that TrxA preferentially binds on the α′ side and more strongly in open $\alpha_2\beta_2$ conformations than in compact conformations (Figures 4A, S10). In our EM maps (Figure S1), only one interfacial residue differs as a function of TrxA binding: F624 from α′ embeds in a hydrophobic pocket of TrxA (Figure 4B-C), whereas F624 in α adopts two rotamer conformations (Figure S11A), one of which conflicts with TrxA binding. MD simulations (Supplementary Materials, Figure S11B), however, suggest that F624 does not play a major role in regulating TrxA's binding preference for oxidized α′.

We next examined whether TrxA binding is affected by the oxidation state of the cysteine pair (C695/C698) on the flexible α C-terminal tail. Previously, we were able to crystallographically trap this α-tail in the *Bs* RNR active site to show that substrate and tail binding are mutually exclusive (*18*). Consistent with its function to dynamically move in and out of the substrate-binding pocket to reduce C170/C409, we do not observe density for the α-tail (residues 688-700) by cryo-EM. Instead, blurred density is observed in the active site that can be attributed to an average of nucleotides and α-tail sampling and competing for the same pocket (Figure S5). To obtain plausible tail conformations, we used AlphaFold2 (*26*) to predict the α′-TrxA complex, with all resulting predictions consistent with EM (root-mean-square deviation of 1.2 Å for the top prediction). Interestingly, in many of the predictions, the α′-tail adopts a conformation in which its two cysteines appear poised to react with the cysteine pair on TrxA, and other tail residues form several polar interactions with TrxA and W623α′ (Figure 4D). To test whether the stability of this interaction is directly related to the oxidation state of C695/C698, we performed MD simulations on the reduced and oxidized states and obtained free energy landscapes along two distances defined between the α′-tail and its binding interface (Methods, Figure S12) via 2D umbrella sampling (Figure 4E). We find that the disulfide bond in the oxidized α′-tail rigidifies the bound conformation, while the reduced α′-tail exhibits increased flexibility resulting in a less-steep pathway to dissociation. Overall, these results suggest that the binding affinity of TrxA is dependent on the oxidation state of the α′ C-terminal cysteines.

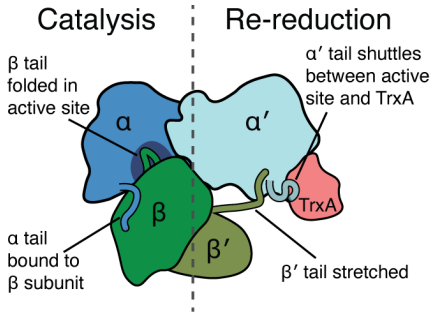

Figure 5. Proposed mechanism behind functional asymmetry in RNR. The $\alpha_2\beta_2$ complex is highly dynamic but always asymmetric about the C2 axis of the α_2 subunit (dashed line), leading to different interactions with the functional α and β C-terminal tails on each side. The β C-terminus binds the tail-binding cleft on both sides of the α_2 subunit, whereas the α C-terminus can interact with the β_2 subunit, the active site, or TrxA, depending on proximity. The α/β side of the complex can close into a PCET-capable conformation where the disordered region of the β tail can reach into the active site along with the substrate. In contrast, on the α′/β′ side of the complex, the β′ subunit is angled away from the α′ subunit, and the α tail is available for shuttling between the active site and TrxA. In order for the α/β and α′/β′ sides to switch, β_2 will need to rotate to the opposite orientation, which likely involves temporary disengagement from α_2.

Finally, we propose a model for how the intrinsic dynamics of RNR leads to functional asymmetry (Figure 5). RNR continuously samples asymmetric conformations, maintaining an α/β (PCET-capable) side and an α′/β′ (PCET-incapable) side. The flexible α and β tails also sample a multitude of conformations even within a single $\alpha_2\beta_2$ pose, but the asymmetry within the complex provides different environments for the tails that shift their conformational ensembles to enable functional steps. The β-tail has two key functions in class I RNRs: to bind the α subunit and to fold into the active site for PCET. The α-tail, on the other hand, must shuffle between the active site and TrxA to fulfill the re-reduction process. Interestingly, it was shown in the structure of the *Ec* RNR complex that the α-tail can interact with the β subunit on the side engaged in PCET, with similar α-tail density observed in some of our EM maps (Figure S13). We thus propose that on the α/β side, the β subunit can approach the α subunit for PCET, and the affinity of the α-tail for the β subunit reduces the interaction of α with TrxA. Such a mechanism would explain the low TrxA occupancy on this side as well as how the α-tail might vacate the active site when the complex approaches the PCET conformation, allowing entry of the β-tail (Figure S7D). In contrast, on the α′/β′ side, the β′ subunit is tilted away from the α′ subunit with its β′-tail stretched across the gap. This arrangement allows the α′-tail to freely move between the active site and TrxA, resulting in increased TrxA interaction and occupancy.

Dynamics have long been recognized to be critical for enzyme function, yet structural characterization of such motions has been challenging to achieve. Here, we performed advanced cryo-EM analyses to directly visualize the conformational landscapes of a class I RNR. We find that the active class I RNR undergoes significant continuous motions while maintaining asymmetry, corroborating an abundance of biochemical evidence for half-site reactivity in both the half cycles of turnover (*9–17*). While structural asymmetry does not necessarily mean that the two halves of the complex must alternate between the two halves of the turnover cycle, it provides an interlock that ensures that PCET only fires when the right constituents are in the active site and protects the α-tail from radical chemistry. As proxies for free energies, these landscapes also allow the visualization of structural dynamics associated with distinct steps detected by enzyme kinetics. Future endeavors, such as time-resolved and single-molecule experiments, may enable validation of conformational landscapes obtained from cryo-EM. Computational methods proposing to extract information from raw particle images, such as MD ensemble reweighting (*27*), also presents an intriguing avenue for overcoming the loss of intrinsically disordered regions, such as the α and β C-termini, during averaging in conventional cryo-EM data processing. Finally, bioinformatic analyses (Supplementary Materials) reveal that the TrxA-binding site identified herein is conserved only in a subset of class I RNRs, which includes those found in certain human pathogens but excludes humans, offering a promising target for drug development.

Data Availability

Cryo-EM maps have been deposited to the Electron Microscopy Data Bank with accession codes EMD-44947, EMD-44985, EMD-44991, EMD-44992, EMD-44995, EMD-44999, EMD-45000, EMD-45004, EMD-45010, EMD-45011, EMD-45014, EMD-45015, EMD-45016, EMD-45017, EMD-45018, EMD-45019, EMD-45020, EMD-45021, EMD-45023, EMD-45024, EMD-45026, EMD-45029, EMD-45030, EMD-45031, EMD-45037, EMD-45044, EMD-45045, EMD-45046, EMD-45047, EMD-45048, EMD-45049, EMD-45051, EMD-45052, EMD-45053, EMD-45054, EMD-45057, EMD-45061, EMD-45064, EMD-45065, EMD-45066, EMD-45067, EMD-45068, EMD-45069, EMD-45070, EMD-45071, EMD-45072. The associated atomic models have been deposited to the Protein Data Bank with accession codes 9bw3, 9bwx, 9bx2, 9bx3, 9bx6, 9bx8, 9bx9, 9bxc, 9bxs, 9bxt, 9bxx, 9bxz, 9by0, 9by1, 9by2, 9by3, 9by7, 9by8, 9by9, 9bya, 9byc, 9byd, 9byg, 9byh, 9byl, 9byt, 9byv, 9byw, 9byx, 9byy, 9byz, 9bz2, 9bz3, 9bz5, 9bz6, 9bz9, 9bza, 9bzd, 9bze, 9bzf, 9bzh, 9bzi, 9bzj, 9bzk, 9bzm, 9bzo. Final cryoDRGN models for the four conditions used in landscape analysis will be deposited to Zenodo. Raw EM data for the four conditions will be deposited to EMPIAR.

Acknowledgments

The authors are grateful to Prof. JoAnne Stubbe (MIT) for sharing plasmids of *Bs* RNR, NrdI, TrxA, and TrxB and many insightful conversations over the years. We are also grateful to Drs. Maxwell Watkins and Steve Meisburger for discussions during an earlier phase of this project and to Prof. Brian Crane (Cornell) for critical reading of this manuscript. Cryo-EM data in this work were collected at the Cornell Center for Materials Research (CCMR), which is supported by the National Science Foundation (NSF) under award DMR-1829070. This work also made use of the National Center for CryoEM Access and Training (NCCAT) and the Simons Electron Microscopy Center located at the New York Structural Biology Center, supported by the NIH Common Fund Transformative High Resolution Cryo-Electron Microscopy program (U24 GM129539) and by grants from the Simons Foundation (SF349247) and NY State Assembly. This work was supported by National Science Foundation (NSF) grant MCB-1942668 and startup funds from Cornell University to N. A.

Author Contributions

N. A. conceived of the project, oversaw and supervised the research, analyzed data, and acquired funding. D. X. performed sample preparation, biochemical characterization, cryo-EM characterization, computation, bioinformatics, and analyses described in this work. W. C. T. prepared *Bs* NrdE and performed analysis of a preliminary EM dataset collected on *Bs* RNR with chemical reductant, and A. A. B. prepared *Bs* TrxB. D. X. and N. A. wrote the manuscript.

Materials and Methods

Protein Expression, Purification and Characterization

NrdE (RNR α subunit), Mn-reconstituted NrdF (RNR β subunit), NrdI (flavodoxin), TrxA (thioredoxin), and TrxB (NADPH-dependent thioredoxin reductase) from *B. subtilis* (*Bs*) were prepared according to published protocols (*20*, *28*, *29*) with key steps and modifications described below. Plasmids containing genes for N-His_6-Smt3-tagged NrdE, N-His_6-tagged NrdF, N-His_6-Smt3-tagged NrdI, N-His_6-tagged TrxA, and N-His_6-tagged TrxB were generously provided by JoAnne Stubbe (MIT). All proteins were expressed in an *E. coli* BL21 derivative (T7 Express, NEB) using Luria Broth (Miller) medium, unless described otherwise. Nickel and cobalt affinity chromatography steps described below were performed with HisPur Ni-NTA resin (ThermoFisher) and TALON cobalt affinity resin (Takara), respectively. All protein concentrations below are given as monomer concentrations.

***Bs* RNR α subunit.** N-terminally His_6-Smt3-tagged NrdE was purified with a nickel affinity column, followed by anion exchange chromatography (HiPrep Q FF 16/10, Cytiva). The His_6-Smt3 tag was cleaved using SUMO protease and separated from tagless NrdE (having only its native sequence) using a second nickel affinity column. We note that *Bs* NrdE, purified at this stage, is partially inhibited by endogenously bound deoxyadenosine 5′-monophosphate (dAMP) (*29*), but its effect is reversed by addition of purine nucleotides, such as adenosine 5′-triphosphate (ATP) and guanosine 5′-diphosphate (GDP) (*18*), which are present in all of the experiments described in this study. Finally, tagless NrdE was exchanged into RNR storage buffer (50 mM HEPES, 150 mM NaCl, 15 mM $MgCl_2$, 5% (w/v) glycerol, pH 7.6) supplemented with 1 mM tris(2-carboxyethyl)phosphine) (TCEP).

***Bs* NrdI.** N-terminally His_6-Smt3-tagged NrdI, used in the reconstitution of NrdF, was purified with a cobalt affinity column, and the tag was cleaved and separated in the same manner as NrdE to produce tagless NrdI (having only its native sequence). Cofactor reconstitution was then performed by incubating ~15 μM tagless NrdI with ~800 μM flavin mononucleotide (FMN) for 4-6 hours before exchanging into reconstitution buffer (50 mM HEPES, 5% glycerol, pH 7.6) to remove free FMN.

***Bs* RNR β subunit.** N-terminally His_6-tagged apo-NrdF was expressed with 1,10-phenanthroline added to the cell culture at a final concentration of 0.1 mM 20 min before induction with isopropyl β-d-1-thiogalactopyranoside (IPTG). His_6-tagged apo-NrdF was then purified with a cobalt affinity column and exchanged into reconstitution buffer. Metal reconstitution of NrdF was performed in a Coy anaerobic chamber under a N_2/H_2 atmosphere (95%/5%) at room temperature. Deoxygenated reconstitution buffer was used to prepare anoxic $MnCl_2$ and $Na_2S_2O_4$ solutions inside the chamber, and apo-NrdF solution was allowed to equilibrate with the chamber atmosphere for an hour. Tagless NrdI was fully reduced to its hydroquinone form with $Na_2S_2O_4$ solution, and a 2-fold molar excess of $MnCl_2$ was mixed with the apo-NrdF solution. Equimolar apo-NrdF and NrdI (quantified by FMN concentration) were used. Both solutions were incubated for 20 min, before the two solutions were mixed and taken out of the Coy chamber. Oxygen-saturated reconstitution buffer was then added at ~2-3 times the volume to the mixture to form the dimanganese tyrosyl radical ($Mn(III)_2$–Y•) cofactor. Mn-reconstituted NrdF (Mn-NrdF) was purified from mismetallated NrdF and NrdI by high-resolution strong anion exchange (Mono Q 10/100, Cytiva) before exchanging into RNR storage buffer. The radical content of Mn-NrdF was determined to be 1.23 Y•/dimer (comparable to previously reported values (*20*, *28*)) with electron paramagnetic resonance (EPR) spectroscopy by comparison to a Fe-reconstituted NrdF sample with known radical content and a 2,2,6,6-tetramethyl-1-piperidinyloxy (TEMPO) standard.

***Bs* RNR reducing system.** N-terminally His_6-tagged TrxA was purified with a cobalt column, followed by size exclusion chromatography (HiLoad 16/600 Superdex 200 pg, Cytiva) in buffer containing 50 mM sodium phosphate, 150 mM NaCl, pH 7.6. Pure fractions were combined and exchanged into RNR storage

buffer. N-terminally His_6-tagged TrxB was expressed, purified, and assayed following published methods (*20*, *28*) with the following modifications. Protein was expressed in BL21-derived C43 *E. coli* cells (OverExpress C43(DE3) cells, Sigma) and induced with 0.4 mM IPTG for 6 hours. Harvested cells were lysed in 50 mM sodium phosphate, 300 mM NaCl, 10 mM imidazole, and 5% (v/v) glycerol, pH 7.6, with 2 mM flavin adenine dinucleotide (FAD), 2 U mL^{-1} DNase, 1 U mL^{-1} RNase A and 0.2 mg mL^{-1} lysozyme. His_6-tagged TrxB was then purified using a cobalt affinity column before exchanging into RNR storage buffer. Flavin adenine dinucleotide (FAD) content was measured to be 1.13 FAD per TrxB monomer following procedures in (*28*). Redoxin activity of His_6-tagged TrxB was assayed using 5,5'-dithiobis-(2-nitrobenzoic acid) (DTNB) as a substrate at 25 ˚C to be 4.75 µmol DTNB (min mg TrxB)$^{-1}$ following procedures in (*28*).

***Bs* RNR activity.** A spectroscopic activity assay was performed with tagless NrdE, His_6-tagged Mn-NrdF, His_6-tagged TrxA, and His_6-tagged TrxB following established protocols (*28*). A reaction mixture containing 1 µM NrdE, 1 µM NrdF, 0.25 mM thymidine 5′-triphosphate (TTP), 1 mM ATP, 0.5 mM GDP, 40 µM TrxA, 0.4 µM TrxB, 0.2 mM nicotinamide adenine dinucleotide phosphate (NADPH) in RNR storage buffer yielded a measured activity of 225 ± 28 U (mg $\alpha_2\beta_2)^{-1}$, comparable to a V_{max} of 220 ± 3 U (mg $\alpha_2\beta_2)^{-1}$ reported in (*28*) with the TTP and GDP effector-substrate pair.

Cryo-EM Sample Preparation and Data Collection

Cryo-EM was performed with tagless NrdE, His_6-tagged Mn-NrdF, His_6-tagged TrxA, and His_6-tagged TrxB using TTP as the specificity effector, ATP as the activity effector, GDP as the substrate, dGDP as the product, and NADPH as the reductant for TrxB. Four different conditions were prepared in RNR storage buffer, all containing 5 µM NrdE, 5 µM NrdF, 30 µM TrxA, 0.25 mM TTP, and 1 mM ATP as common ingredients, and the concentrations of substrate, product, TrxB, and NADPH were varied to capture different stages of enzymatic turnover.

To prepare the turnover condition, all ingredients but the substrate were pre-mixed in one tube (40 µL), while GDP was kept in a separate tube as a 200 µM stock solution. Both solutions were equilibrated at room temperature for 5 mins before the reaction was initiated by adding 10 µL of GDP solution through repetitive pipetting to obtain a reaction mixture of the common ingredients supplemented with excess GDP (0.5 mM) as well as high levels of TrxB (1 µM) and NADPH (1 mM) to ensure sufficient reduction speed. Sample was frozen within 20 s after reaction initiation. Based on the enzyme activity, we estimate that less than 10% of GDP had turned over in 20 s, and therefore consider this condition to be representative of active turnover. The pre-turnover condition was prepared by including 0.4 µM TrxB and 1 mM NADPH with the common ingredients, while omitting the substrate GDP from the mixture. The product condition was prepared by including 0.4 µM TrxB, 1 mM NADPH, and 0.5 mM dGDP with the common ingredients. To prepare the pre-reduction condition, the common ingredients were supplemented with 0.5 mM GDP, 0.4 µM TrxB, and limiting NADPH (0.1 mM). The sample was incubated at room temperature for 3 min (at which point, our calculations indicate that NADPH would be well depleted but <20% of the substrate would be converted to product) before freezing. We thus consider this condition to representative of a state where the RNR α subunit (active site and C-terminus) and TrxA/TrxB are oxidized and awaiting re-reduction by NADPH before another round of turnover can begin.

All cryo-EM grid freezing was performed on an FEI Vitrobot Mark IV with the chamber humidity set to 100% and the temperature set to 25°C. QuantiFoil holey carbon R 1.2/1.3 300-mesh copper grids were used for all samples, which were glow discharged on a PELCO easiGlow system for 45 s with 20 mA current prior to sample application. Four µL of sample was applied onto the grid, and the grid was then blotted for 3.5 s and immediately plunge frozen in liquid ethane cooled by liquid nitrogen.

Datasets for all conditions shown in this work were collected on a Talos Arctica (Thermo Fisher Scientific) at the Cornell Center for Materials Research (CCMR). The microscope operates at 200 keV with a Gatan K3 direct electron detector and BioQuantum energy filter (20 eV slit width) at a nominal magnification of 79,000× (nominal pixel size of 1.04 Å $pixel^{-1}$). Movies were collected with a nominal defocus range from –0.8 to –2.0 µm and a total dose of 50 $e^- Å^{-2}$ over 50 frames, with a 3 x 3 multishot scheme in SerialEM (*30*). Total numbers of movies collected for each condition are: 4537 for the turnover condition, 3476 for the pre-turnover condition, 3503 for the product condition, 4410 for the pre-reduction condition. The exposure time, frame time, and dose rate for each condition were: 2.23 s, 0.0445 s, and 22.60 $e^- Å^{-2} s^{-1}$ for turnover condition; 2.031 s, 0.0405 s, and 24.77 $e^- Å^{-2} s^{-1}$ for pre-turnover condition; 2.164 s, 0.0435 s, and 22.98 $e^- Å^{-2} s^{-1}$ for product condition; 2.031 s, 0.0405 s, and 24.61 $e^- Å^{-2} s^{-1}$ for pre-reduction condition.

Recent computational work estimates that energy barriers higher than 10 kJ mol^{-1} (2.4 kcal mol^{-1}) are not crossed during the rapid cryo-cooling of cryo-EM grids (*31*), which is lower than many energy barriers between side chain rotamer conformations. We thus interpret the cryo-EM datasets in this work with the assumption that the conformational ensemble of β subunit is preserved through cryo-cooling.

Cryo-EM Data Processing

Datasets for all four conditions were processed individually through similar workflows in cryoSPARC 4 (*32*) and RELION 4 (*33*). Movies were first motion-corrected either in RELION 4 using RELION's implementation of MotionCorr2 with 7 x 5 patches (pre-turnover and pre-reduction datasets) or in cryoSPARC with patch motion correction (turnover and product datasets). Dose-weighted micrographs motion-corrected in RELION 4 were imported into cryoSPARC. Patch CTF estimation was then performed on micrographs in cryoSPARC to obtain the CTF parameters. Micrographs were then filtered with a CTF fit resolution cutoff of 5 Å and inspected manually to further exclude bad micrographs. Particle picking was then performed with Topaz (*34*) using a pretrained ResNet16 model and extracted with a box size of 256 x 256 pixels Fourier cropped to 128 x 128 pixels. 2D classification was performed on extracted particles, and particles corresponding to classes containing secondary structural details were kept. Kept particles were further filtered with a class probability cutoff of 0.99, and the top 400 - 600 micrographs with the most remaining particles were used as training data to train a Topaz ResNet8 model initialized from pretrained weights. The trained model was used to perform the final particle picking from micrographs, and resulting particles were then extracted with a box size of 256 x 256 pixels Fourier cropped to 128 x 128 pixels. 2D classification was performed on extracted particles, and particles from low quality 2D classes were excluded from further processing. *Ab initio* reconstruction and homogeneous refinement were performed on kept particles, and duplicated particles with separation distance below 40 Å were removed. This process resulted in 1.011M particles on 3258 micrographs for the turnover condition, 893K particles on 2532 micrographs for the pre-turnover condition, 991K particles on 2777 micrographs for the production condition, and 552K particles on 3785 micrographs for the pre-reduction condition (Table S1).

Micrographs initially motion-corrected in cryoSPARC were motion-corrected again in RELION 4. Particle coordinates from cryoSPARC were converted to RELION star format with pyem (*35*), and particles were re-extracted from the motion-corrected micrographs in RELION 4 with a box size of 256 x 256 pixels. 3D auto refine was performed on particles, followed by CTF parameter refinement (anisotropic magnification, beam tilt, trefoil, spherical aberration, per-micrograph astigmatism, and per-particle defocus), with particles split into 9 optics groups based on the 3 x 3 multishot position of their originating micrographs during collection. Bayesian polishing parameters were then trained with 8000 particles, with which two iterations of processes consisting of Bayesian polishing followed by CTF refinement were performed to obtain polished shiny particles. The shiny particles were imported into cryoSPARC to perform one to two rounds of multi-class *ab initio* reconstruction and heterogeneous refinements into five classes. Particles from classes in which the β_2 density does not resemble an intact β_2 were excluded. This particle-filtering process led to 597K particles for the turnover condition, 667K particles for the pre-turnover condition, 455K for the

product condition, and 368K particles for the pre-reduction condition, which were used for 3D classification in RELION 4 (Figures S14, S16, S18, S20 red path), described in detail below.

An additional round of heterogeneous refinement was performed to ensure that we include as many good particles while excluding as many bad particles as possible from the datasets, producing a slightly different set of particles for cryoDRGN analyses (Figures S14, S16, S18, S20 blue path). True pixel sizes were first estimated through comparison of the spherical aberration obtained from CTF parameter refinement (with a single optics group) to the true value of the instrument (2.7 mm), resulting in the following values: 1.017 Å for the turnover dataset, 1.022 Å for the pre-turnover dataset, 1.017 Å for the product dataset, and 1.014 Å for the pre-reduction dataset. CTF parameters for kept particles were re-estimated after pixel size correction, and homogeneous refinement followed by non-uniform refinement (*36*) were finally performed in cryoSPARC to generate the consensus map for each condition. The sharpened map from this consensus refinement (Figures S14, S16, S18, S20, purple triangle) was used to build and refine atomic models of the α_2 bound with the β C-terminal tail for each condition (Table S1). This resulted in cryoDRGN particle sets consisting of 596K particles for the turnover condition, 666K particles for the pre-turnover condition, 505K for the product condition, and 361K particles for the pre-reduction condition (Table S1).

For the pre-reduction condition, focused classification of TrxA was performed in cryoSPARC on the 552K particle set (Figure S20) with a mask created in ChimeraX (*37*) by using the molmap function to generate a map of an AlphaFold2 (*26*) model of TrxA docked in the EM map at 20 Å resolution and then thresholded at 0.1. Two rounds of 3D classification into 10 classes were performed, and particles from classes that show high TrxA occupancy were combined (171K particles). Homogeneous refinement and nonuniform refinement were performed on those particles, and the resulting half-maps were sharpened with deepEMhancer (*38*) using the tightTarget model (Figure S21B, Table S2).

Analysis of Conformational Changes via 3D Classification

Particle sets described above were imported into RELION 4 to perform discrete 3D classification individually for each condition (Figures S14, S16, S18, S20 red path). 3D auto refine was performed on imported particles, followed by CTF parameter refinement to produce the consensus reconstruction. A spherical mask with a radius of 40 Å encompassing the β_2 region was used to perform particle subtraction and remove α_2 signal from particle images. 3D classification without alignment into 20 classes was then performed focused on the β_2 region with subtracted particles and the spherical mask. Due to the pseudosymmetry of the class I RNR complex (where the major signal for alignment comes from the larger, symmetric α_2 while the asymmetrically posed β_2 contributes less to alignment), a small population of β_2 aligning in the opposite direction was observed in the 3D classification result. In order to minimize their occurrence, an additional consensus reconstruction was performed using a reconstructed 3D class with β_2 well-resolved and in a compact conformation as a reference map. The consensus map resulting from this step was also used in rigid-body docking that yielded the consensus full-complex models of RNR for each condition (Figures S14, S16, S18, S20 green square, Table S2). Particle subtraction and 3D classification were performed on the new consensus reconstruction in the same fashion as before. Subtracted particles from classes with β_2 density agreeing with the β_2 model, which generally featured clear secondary structures (largely helical), were reverted to original particles and reconstructed individually for each class (Figures S14, S16, S18, S20, Table S2). This yielded 8 classes for the turnover condition, 5 classes for the pre-turnover condition, 8 classes for the product condition, and 3 classes for the pre-reduction condition.

Conformational Landscape Analysis in CryoDRGN

Preparation of particles for CryoDRGN. To prepare particles for cryoDRGN analysis (which does not allow multiple optics groups and higher order aberration corrections), particle sets described above (Figure S14, S16, S18, S20 blue path) were collapsed into a single optics group for every condition, and CTF

parameters were re-estimated with only per-particle defocus optimization in cryoSPARC. In order to align poses of particles from all conditions, which are of different pixel sizes, particles were imported to RELION 4 with each condition consisting of one optics group, and a consensus reconstruction combining particles from all conditions was performed with a compact state from the pre-reduction condition (Figure S22) as the reference map. To further filter particles that have misaligned β_2 (due to pseudosymmetry) or do not contain β_2, focused 3D classification without alignment was performed on the all-condition combined refinement with particle subtraction of the α_2 signal (as described above) to generate 50 classes. Particles from classes with β_2 aligning to the opposite direction, or with density unresembling β_2, were discarded (16 classes out of 50 classes, 442K particles out of 2.127M particles). Further 3D classification of discarded particles did not yield better resolved classes. Subtracted particles from kept classes were then reverted to original ones. 13 classes with well-resolved β_2 density were reconstructed individually (Figure S22 black boxes, Table S2). Particles from all kept classes were then split into individual conditions to perform cryoDRGN analysis on each condition individually. This led to individual sets of 476K particles for the turnover condition, 536K particles for the pre-turnover condition, 406K particles for the product condition, and 287K particles for the pre-reduction condition.

Training cryoDRGN models and particle filtering. CryoDRGN version 2.3 was used to perform the analyses. For each dataset, particles were first downsampled to a box size of 128 x 128 (~2.04 Å pixel size) and preprocessed to the Fourier space representation. Then an 8D latent variable cryoDRGN model with 1024 x 3 encoder and decoder dimensions was trained for 50 epochs. UMAP embeddings of the latent space representation were inspected, and particles in clusters corresponding to junk particles were removed (Figures S24-S27, blue clusters in top right plot). The remaining particles were used to train a second latent variable model with the same parameters as the first one, and a *k*-means clustering with *k*=50 was performed to generate 50 cluster volumes for visual inspection. Particles from clusters where the β_2 density did not resemble an intact β_2 were excluded. A third latent variable model was then trained on the kept particles, from which a *k*-means clustering with *k*=1000 was performed to generate 1000 cluster volumes. To efficiently and objectively filter particles with poor β_2 density, the following procedure was used. An α_2 model refined against the pre-turnover consensus map and a β_2 crystal structure from PDB entry 4dr0 (*19*) (with residues before Thr18 removed) were rigid-body docked into each volume in ChimeraX using a custom script. Briefly, initial configurations of α_2 and β_2 used in docking were those from the consensus map of the all-condition combined refinement. α_2 was first docked into its density, after which its expected map was generated with molmap at Nyquist resolution and subtracted from the cluster volume. Then the subtracted volume was thresholded by a level computed as the mean plus 0.25 times the difference between maximum and mean intensity of all voxels, to minimize the effect from "hot voxels" that we observe in certain cluster volumes. Finally, the β_2 model was docked in the subtracted and thresholded map. After docking, binary masks for each subunit were then generated using the molmap command with 20 Å resolution and thresholding at a level of 0.1. An "occupancy" value was calculated for β_2 in a similar fashion to previous work (*23*), where the ratio of average voxel intensities within the β_2 and α_2 masks was compared to the expected ratio for full occupancy from a volume generated with the molmap command in ChimeraX at Nyquist-limit resolution (~4.08 Å). For each volume, the number of connected voxels for all overlapping regions between α_2 and β_2 masks were computed, and the largest value among those was used as an "overlap score". After visually inspecting various cutoff values, we used a β_2 "occupancy" cutoff of 0.65 and an "overlap score" cutoff of 150 to reasonably filter clusters with poor β_2 density from the 1000 cluster volumes. Principal component analysis (PCA) of the latent space representation was used to further filter particles with poor β_2 density in two datasets at this iteration. For the turnover condition, particles with principal component PC2 higher than 0.25 were excluded, while for the pre-reduction condition, particles with principal component PC1 lower than -0.25 were excluded. After all rounds of filtering, the numbers of remaining particles were 255K for the turnover condition, 286K for the pre-turnover condition, 246K for the product condition, and 128K for the pre-reduction condition. A final latent variable model was then trained on the kept particles that yielded the final cryoDRGN model used in landscape analysis. Volumes

along the first two principal components of the final cryoDRGN models for all four conditions are animated as movies (Movies S1-S4).

Landscape analysis. Landscape analysis was performed on the final cryoDRGN model with 1000 clusters. Following the same procedure described above for the third filtering step, α_2 and β_2 models were rigid-body docked into the cluster volumes, and the β_2 "occupancy" and $\alpha_2\beta_2$ "overlap score" were calculated for each. Cluster volumes were filtered with a β_2 "occupancy" cutoff of 0.7 and a "overlap score" cutoff of 150, which resulted in the following number of clusters and particles for subsequent analyses: 863 clusters consisting of 225K particles for the turnover condition, 727 clusters consisting of 212K particles for the pre-turnover condition, 801 clusters consisting of 199K particles for the product condition, and 858 clusters consisting of 113K particles for the pre-reduction condition.

To parametrize the inter-subunit orientation in each cluster, coordinate systems were defined for the docked models of α_2 (xyz) and β_2 ($x'y'z'$), and the rigid-body transformation between them was calculated, where the rotation operation was calculated using SciPy (*39*). For the discussion below, the chain names of the modeled $\alpha_2\beta_2$ complex can be visualized in Figure S28A (note that chains A and B of the docked 4dr0 crystal structure were renamed to C and D, respectively).

The first coordinate system was defined as centered on the center of mass (COM) of α_2, with the y-axis defined as the unit vector in the direction of the C2 axis of α_2, calculated by finding the intersecting line between the plane formed by the Cα atoms of residue 180 in each monomer and the dimer COM, and the plane formed by the Cα atoms of residue 190 in each monomer and the dimer COM. The z-axis was defined as the cross product between the y-axis and the vector between the dimer COM and the Cα atom of residue 308 in chain A of α_2. The x-axis was then defined by taking cross product of the y-axis and z-axis.

The second coordinate system was defined as centered on the COM of β_2, and the y'-axis is defined as the unit vector in the direction of the C2 axis of the β_2, calculated by finding the intersecting line between the plane formed by the Cα atoms of residue 111 in each monomer and the dimer COM, and the plane formed by the Cα atoms of residue 215 in each monomer and the dimer COM. The z'-axis is defined as the cross product between the y'-axis and the vector between dimer COM and the Cα atom of residue 179 in chain D of β_2. The x'-axis was then defined by taking cross product of the y'-axis and z'-axis.

The inter-subunit orientation was then parametrized as a 7D coordinate describing the transformation between the two coordinate systems, which includes the translation vector (3D) between the COMs of the α_2 and β_2 in the first coordinate system and the quaternion (4D) that describes the rotation needed to match the orientation of first coordinate system to the second. For each model, the distance between the Cα atoms of two residues involved in inter-subunit radical transfer, Y684 in chain A in α_2 and W30 in chain C in β_2, was calculated. Euler angles ψ, θ, φ corresponding to extrinsic rotation with about the x-y-z axes (Figure S28B) were also calculated. Notably, Euler angle φ is correlated with the "openness" of β_2 relative to α_2, while Euler angle ψ is correlated with the asymmetric posing of β_2.

To visualize the conformational landscapes of β_2, DensMAP (*24*) was employed to embed the 7D coordinates of β_2 obtained above onto two dimensions. To quantify the similarity of any two β_2 conformations in the embedding process, we defined the distance metric as the sum of distance between the two β_2 COMs (in Angstroms) and the angle of rotation between the two quaternions (in degrees). An n_neighbors value of 50 was used. The β_2 coordinates from all four datasets, as well as coordinates of β_2 from 3D classes obtained in RELION, were combined to produce a single joint embedding (Figure S8A, Table S3). To test the stability of the resulting embeddings, the DensMAP calculation was performed with 100 different random seeds (Figure S29). While the majority of the embedding was very stable, the embedding around the PCET-like region showed slight variations due to the smaller population. We thus chose a representative embedding (random state 64) for further analysis, based on direct knowledge of the

similarity of individual classes in the PCET-like region. The embedded β_2 coordinates from the joint embedding (random state 64) were then separated by condition to produce the 2D representation for each condition (Figure S8B-C). Gaussian kernel density estimation was performed to estimate the 2D probability distribution of each conformational landscape, with the number of particles in each cluster used as weights. The smoothing bandwidth used during estimation was calculated with Scott's Rule (*40*) for the combined embedding, and a fixed value of 0.328 (equivalent to 800 data points with Scott's Rule) for the individual conditions.

To verify that a *k*-means clustering with *k*=1000 sufficiently samples the latent space, we repeated the landscape analysis from trained cryoDRGN models with a smaller number of clusters (*k*=500). The resulting representation (Figure S30) is consistent in terms of topology, 3D class locations, and the estimated landscape, suggesting that our sampling with *k*=1000 is sufficient.

TrxA occupancy for each cluster volume was calculated in a manner similar to the β_2 occupancy calculation described above. Binary masks for TrxA on each side were generated from docked atomic models using the molmap command with 20 Å resolution and thresholding at a level of 0.1. Occupancy values were then calculated as the ratio of average voxel intensities within the TrxA and α_2 masks divided by the expected ratio for full occupancy from a volume generated with the molmap command in ChimeraX at Nyquist-limit resolution (~4.08 Å).

Cryo-EM Model Building and Refinement

For every condition, the sharpened consensus map (Figures S14, S16, S18, S20 purple triangle) showed strong density for residues 311 - 322 of the β C-terminal tail bound to the back of each monomer in α_2, with the turnover and product maps showing reasonable density for two additional residues, 309 and 310. Thus, for each condition, consensus models of α_2 with bound β C-termini was refined using real-space refinement in Phenix (*41*, *42*) with the AlphaFold2 (*26*) model of monomeric α subunit obtained from UNIPROT (*43*) entry P50620 as the starting structure. Two copies of the monomeric α subunit model were rigid-body fit into the cryoSPARC consensus map in ChimeraX, and the ligands and bound β C-terminus were then built manually in COOT (*44*). *Bs* RNR is known to have three allosteric sites: the S-site, which determines substrate specificity, and the I- and M-sites, which together control the overall activity of the enzyme (*18*, *29*). For all conditions, Mg^{2+}-TTP was modeled at the S-site, and an ATP was modeled at the I-site. For the pre-turnover condition, no nucleotide density was observed at the purine-preferring M-site, indicating that ATP does not bind strongly here. Therefore, for the turnover and pre-reduction conditions, a GDP was modeled at the M-site, which was consistent with the density. For the product condition, a dGDP was modeled at the M-site. The restraint file for dGDP was generated using the Grade2 server (*45*). The nucleotide density in all refined structures can be visualized in Figure S31. The initial models were refined against the cryoSPARC unsharpened consensus map and then against the sharpened map, after which the atomic model was inspected in COOT to fix issues manually, as well as removing terminal residues with poor density (residues 1 – 5 and 689 – 700 in α_2). The density around the active-site cysteine pair (C170/C409) was also inspected (Figure S4); the pre-turnover and product conditions show clearly reduced density, while the pre-reduction shows strong density for a disulfide bond, and the turnover condition shows a mixture between oxidized and reduced density. We thus modeled a disulfide bond between C170 and C409 in COOT for the pre-reduction condition, while the pair was kept reduced in the other conditions. Finally, one or two rounds of real-space refinement against the sharpened map was performed to produce the 4 final consensus atomic models of α_2 bound with nucleotides and β C-termini (Table S1).

Because of the lack of atomic detail in the β_2 and TrxA density, full-complex models were built for every 3D class (37 total, shown in Figure S6) and unsharpened consensus maps (Figures S14, S16, S18, S20, green square) by rigid-body docking atomic models of α_2, β_2, and TrxA into the unsharpened maps obtained from RELION 3D auto refine (Table S2). For maps from each condition, the corresponding consensus

model of α_2 with bound β C-termini and ligands was used in docking. For 3D classes from the all-condition combined refinement, the consensus α_2 model from the turnover condition was used. For β_2, residues 16 – 290 and the dimanganese center in both chains from PDB entry 4dr0 were used in docking (with chains A and B renamed to C and D). Residues 19 – 104 of TrxA in the top-ranking model of the AlphaFold2 multimer prediction of the α/TrxA complex were used for docking in maps containing strong TrxA density (turnover consensus full-complex model and all models from the pre-reduction condition). For each full-complex model, clashes at the interfaces between different chains were fixed by either using ISOLDE (*46*) or by alternating side-chain rotamers.

All-Atom Molecular Dynamics (MD) Simulations and Umbrella Sampling

Umbrella sampling, an enhanced sampling technique for MD, was performed to investigate the molecular mechanisms for preferential binding of TrxA to one side of α_2 in the *Bs* RNR active complex. Two hypotheses were tested. First, we tested whether the flexibility of the interfacial F624α may be coupled to the asymmetry of the $\alpha_2\beta_2$ complex or the oxidation state of the active-site cysteines (C170/C409). The free energy profiles along the rotamer χ_1 angle of F624 obtained by umbrella sampling reveal no significant dependence on the oxidation state of the active-site cysteines or the side of the α_2 dimer (Figure S11B), suggesting that F624 does not play a major role in regulating TrxA's binding preference for oxidized α′. Second, we tested whether the oxidation state of the α C-terminal tail affects TrxA binding. For both tests, methods are detailed below. All preparation and MD simulation for in this work were performed in AmberTools23 (*47*) and Amber22 (*48*).

Starting models for F624 χ_1 umbrella sampling. To examine the dynamics of residue F624 in α at the TrxA binding interface, MD simulations were performed using starting structures produced by docking a consensus atomic model of α_2 bound with β C-termini and the β_2 crystal structure (PDB: 4dr0) into the map of pre-reduction class 11 (Figure S6D), which displays an open conformation with strong TrxA density. For the starting structure representing the oxidized state, the α_2 consensus model from the pre-reduction condition was used (where a disulfide bond is formed between C170 and C409 in both active sites), while for the reduced state, the consensus α_2 model from the pre-turnover condition was used (where the C170/409 pair is modeled as reduced in both active sites). Nucleotide ligands at the M- and I-sites were removed as their physiological roles are to prevent filament formation (which is irrelevant in this simulation), while Mg^{2+}-TTP was kept at the S-site because of its essential role in dimer formation. Modeller (*49*) was then used to build unmodeled regions. Both α C-terminal tails were manually moved away from the TrxA binding interface in COOT as transient interactions between the C-termini and the TrxA binding interface were observed in many of our MD runs (results not shown). For the oxidized state, a disulfide bond was also manually introduced between C695 and C698 in both α C-termini using COOT.

Starting model for 2D umbrella sampling of α-TrxA interactions in oxidized-tail condition. To examine how the oxidation of the α C-terminus may modulate the interactions between α and TrxA, a starting structure was produced by docking the AlphaFold predicted α/TrxA complex, an additional copy of the α subunit from the predicted α/TrxA complex, and the β_2 crystal structure (PDB: 4dr0) into the map of pre-reduction class 11 (Figure S6D). Two copies of Mg^{2+}-TTP and bound β C-terminal tails were added to the model by aligning the α_2 consensus structure from the pre-turnover condition. Modeller was then used to build unmodeled regions. A disulfide bond was manually introduced between C695 and C698 in both α C-termini using COOT. Cysteines in TrxA and α_2 active sites were kept reduced.

Parametrization of TTP. The TTP pdb file was obtained from the starting structure, and hydrogen atoms were added with the reduce command. The antechamber (*50*) command then was used to generate the mol2 file for TTP with GAFF2 (*51*), after which the parmchk2 command was used to generate the frcmod file containing all parameters. Following procedures in the literature (*52*), we modified the partial charges of TTP in the mol2 file in the following fashion. Partial charges for the thymine base and deoxyribose were

obtained from the Amber library, while those for the phosphate tail were obtained from a previous work (*53*). We then subtracted an equal and small amount of charge from every atom to achieve the correct total charge (-4). We also modified the parameters of the phosphate tail in the frcmod file with those reported in the literature (*53*).

Parametrization of the Metal Cofactor in β_2. Because of the absence of crystal structures of *B. subtills* β_2 with the active $Mn(III)_2$–Y• cofactor, we parametrized the cofactor as $Mn(II)_2$ with a protonated tyrosine (Y105β) which is consistent with the experimental condition for PDB entry 4dr0 (*19*). We assumed that because β_2 is not closely engaged with α_2 in the configurations that we sample in MD, an inactive cofactor form in β_2 should have minimal impact on the dynamics of interest within α_2. Modeling was performed based on the metal center in chain B of 4dr0. Water molecules were not included during parametrization of the metal center. The MCPB.py program (*54*) was used to perform the parametrization. For input, a total spin of 11 (11/2 for each Mn^{2+} ion) was used, a cutoff distance of 2.8 Å was used, and large_opt was set to 1 to optimize the hydrogen positions of the large model. Quantum chemical calculations were performed with GAMESS-US (*55*) using the input files generated by MCPB.py. We parametrized both metal sites in β_2 with the obtained parameters including atomic partial charges and force constants.

Preparation and parametrization of starting structures. All starting structures were prepared in the following fashion. Residue names of cysteines involved in disulfide bonds were manually changed to CYX in the pdb file. Protonation states of histidine were then checked with the H++ server (*56*), and residue names were edited accordingly. LEaP was then used to parametrize the structures and generate the topology and initial coordinate files. The ff19SB force field (*57*) was used to model the proteins. Disulfide bonds were formed between corresponding sulfur atoms. TTP and the manganese cofactor were modeled with parameters stated above. The Mg^{2+} ion coordinating the triphosphate of TTP was modeled as an unbound ion. The OPC water model (*58*) along with the matching Li-Merz 12-6 ions model (*59*, *60*) were used. The system was solvated in a periodic truncated octahedron box, with at least 10 Å of water from the protein surface to the box edge. The net charge of the protein (-48 for α_2/β_2, -56 for α_2/β_2/TrxA) was neutralized by addition of Na^+ counterions. Additional Na^+ and Cl^- ions were added to reach a concentration of 150 mM NaCl, and additional Mg^{2+} and Cl^- ions were added to reach a concentration of 15 mM $MgCl_2$. The systems contained ~280K atoms for α_2/β_2 and ~380K atoms for α_2/β_2/TrxA.

Relaxation and equilibration of systems. For all simulations, a Langevin thermostat with a collision frequency of 1 ps^{-1} was used for temperature control, while the Monte Carlo barostat (*61*) was used for pressure control with a target pressure of 1 bar. A cut-off distance of 10 Å was used for nonbonded interactions. The SHAKE algorithm (*62*) was used to constrain bond lengths involving hydrogen atoms. Minimizations were performed with pmemd.MPI, while MD simulations were performed with pmemd.cuda (*63*, *64*). All systems generated from starting models were relaxed and equilibrated in the same fashion. First, the systems are minimized with 5000 cycles of steepest descent with all atoms restrained with a 100 kcal mol^{-1} $Å^{-2}$ force constant. The systems are then gradually heated up from 100 K to 310 K over 1 ns with a 1 fs time step under the NVT ensemble while restraining protein and ligand atoms with a 100 kcal mol^{-1} $Å^{-2}$ force constant. This was followed by two rounds of relaxation at 310 K over 1 ns with a 1 fs time step under the NPT ensemble, with a restraining force constant of 100 kcal mol^{-1} $Å^{-2}$ for the first round and 10 kcal mol^{-1} $Å^{-2}$ for the second round on protein and ligand atoms. The protein side chains were then minimized along with solvent with 2000 cycles of steepest descent followed by 3000 cycles of conjugate gradient, while a 10 kcal mol^{-1} $Å^{-2}$ force constant was used to restrain the backbone atoms and ligand TTP. The protein atoms were then relaxed through three rounds of simulation at 310 K over 1 ns with a 1 fs time step under the NPT ensemble, with decreasing restraining force constraints of 10 kcal mol^{-1} $Å^{-2}$, 1 kcal mol^{-1} $Å^{-2}$, and 0.1 kcal mol^{-1} $Å^{-2}$, applied to the backbone atoms and ligand TTP. Finally, the systems were relaxed with a simulation at 310 K over 1 ns with a 1 fs time step under the NPT ensemble with no restraint to produce the relaxed configuration. The relaxed configuration was further equilibrated at 310 K for 20 ns with a 2 fs time step under the NPT ensemble to produce the initial configurations used for production runs.

Root-mean-square deviations (RMSDs) of the 20 ns unconstrained equilibration runs are plotted in Figure S32, showing that individual protein components were well-equilibrated after 10 ns in all runs, although the full complex exhibited larger deviations due to the flexible tails and drift in orientation between α_2 and β_2.

Umbrella sampling for F624 χ_1 angle. We performed umbrella sampling (*65*) on the χ_1 angle of F624 on both sides of α_2, and with both oxidized and reduced active-site cysteines in α_2. The four sets of umbrella sampling were performed in an identical fashion. Simulations were run at 310 K under the NVT ensemble with a time step of 2 fs. During all simulations, a weak restraining force constant of 0.01 kcal mol^{-1} Å^{-2} was applied to the Cα atom of residues in rigid parts of α_2 (residues 8-685) and β_2 (residues 18-271) as well as the α C-terminal tails (residue 686-700), in order to prevent the complex from drifting away from the initial β_2 configuration and to prevent the α C-terminal tails from transiently interacting with the TrxA binding interface (α C-terminal tails are far away from the interface in the initial configurations used). A total of 72 simulation windows were performed, spanning 360° with an increment of 5°. The χ_1 angle observed in the initial configuration (-60° or -180°) was used as the angle restraint for the first window. The starting structure for equilibration in each window was updated every 6-window batch (30°). The initial configuration was used as the starting structure for the first 6 windows, while an equilibrated configuration from the last window of the preceding 6-window batch was used as the starting structure for the subsequent 6-window batch. An angle restraint force constant of 200 kcal mol^{-1} rad^{-2} was used. For each window, the system was first equilibrated under restraint for 5 ns, after which the χ_1 angle of F624 was recorded every 10 fs for 15 ns. A total sampling of 1.44 μs was performed for each set of umbrella sampling. Histograms of sampled angle in each window are plotted in Figure S33, which shows sufficient overlap between windows. The free energy profiles were reconstructed with the weighted histogram analysis method (WHAM) (*66*). Reconstruction was performed from -65° to 300° with 360 bins and a convergence tolerance of 0.0001.

Initial configuration for 2D umbrella sampling of α tail in reduced-tail condition. In order to keep initial configurations as close as possible between oxidized-tail and reduced-tail conditions, we generated the initial configuration for the reduced-tail condition from the equilibrated oxidized-tail configuration. The equilibrated configuration of the oxidized-tail condition was converted to a pdb file using CPPTRAJ (*67*) including water and ions, in which oxidized CYX residues (C695 and C698) were renamed to CYS residues. LEaP was used to convert this pdb file back into the topology and coordinate files, and the PARMED program (*68*) was used to set the box parameters in the files to those of the equilibrated oxidized-tail configuration. This configuration was first minimized with 2000 cycles of steepest descent followed by 3000 cycles of conjugate gradient, while a 10 kcal mol^{-1} Å^{-2} force constant was applied on all protein and ligand atoms except for the side chain atoms of C695 and C698 on α_2. The minimized configuration was then relaxed with 1 ns simulation with 1 fs time step at 310 K under the NPT ensemble, while a weak restraining force constant of 0.01 kcal mol^{-1} Å^{-2} was applied to the Cα atom of residues in rigid parts of α_2 (residues 8-685), β_2 (residues 18-271), and TrxA (residues 19-103). The resulting configuration was used as the initial configuration for 2D umbrella sampling of the reduced-tail condition.

2D umbrella sampling for α tail. We performed 2D umbrella sampling on the α C-terminal tail in the TrxA bound conformation with both oxidized and reduced α C-terminal tails in an identical fashion. Simulations were run at 310 K under the NVT ensemble with a time step of 2 fs. During simulation, a weak restraining force constant of 0.01 kcal mol^{-1} Å^{-2} was applied to the Cα atom of residues in rigid parts of α_2 (residues 8-685), β_2 (residues 18-271), and TrxA (residues 19-103), in order to prevent the complex from drifting away from the initial β_2 configuration. 2D umbrella sampling was performed on two distances defined between the α C-terminal tail and its binding interface with TrxA (Figure S12). The COM of the binding interface was defined as the COM of Cα atoms of W623 on α and S71, I72 and G89 on TrxA. Distance 1 was then defined as the distance between the Cα atom of S697 on α and the COM of the binding interface. Distance 2 was defined as the distance between the COM of Cα atoms of C698 and V699 on α,

and the COM of the binding interface. We sampled distance 1 from 4.0 Å to 8.5 Å in 10 windows (0.5 Å increment) and distance 2 from 5.5 Å to 10 Å in 10 windows (0.5 Å increment), resulting in a total of 100 windows. The first window (with window centers of 4.0 Å and 5.5 Å) used the initial configuration as its starting model for equilibration, while subsequent windows used the equilibrated configuration from a window adjacent to themselves as the starting structure. A force constant of 7 kcal mol^{-1} $Å^{-2}$ was used for both distance restraints. For each window, the system was first equilibrated under restraint for 5 ns, after which the two distances were recorded every 20 fs for 25 ns. A total sampling of 3 μs was performed for each set of 2D umbrella sampling. 2D histograms of sampled distances were visually inspected, and regions of low sampling were subjected to two additional sampling windows centered at (distance 1, distance 2) = (5.75 Å, 7.25 Å) and (7.75 Å, 5.75 Å) for the oxidized tail and (6.25 Å, 6.75 Å) and (6.25 Å, 7.0 Å) for the reduced tail with a higher force constant restraint (10 kcal mol^{-1} $Å^{-2}$). The final 2D histograms, plotted in Figure S34, display sufficient distance sampling. The 2D free energy profiles were then reconstructed from 102 windows with WHAM, from 4.0 Å to 8.5 Å for distance 1 and 5.0 Å to 10.0 Å for distance 2, with 100 bins in both dimensions, and a convergence tolerance of 0.0001.

Phylogenetic and Bioinformatic Analyses of TrxA-α Interactions in Class I RNRs

A defining feature of the TrxA-α interface observed in our work is the presence of three consecutive aromatic residues in the α subunit (WFF in the case of *B. subtilis* enzyme) (Figure 4B). When we examine the alignment of class I α sequences from a previously published phylogeny (*2*), we find that 305 out of 2022 sequences contain an aromatic residue at the F624-equivalent position. Additionally, 274 out of those 305 sequences contain at least one additional aromatic residue adjacent to the F624-equivalent position. When we map these sequences onto the tree (Figure S35), we find that they cluster in distinct regions classified as NrdAh and NrdE. Interestingly, the interfacial aromatic residues are only present in one subclade of NrdE (which contains *B. subtilis*) but not the other. To corroborate this finding, we performed AlphaFold multimer predictions for TrxA-α pairs from various organisms, including *Aquifex aeolicus* (NrdAh), *Chitinivibrio alkaliphilus* (NrdAh), *E. coli* (NrdAg), human (NrdAe), and *Salmonella typhimurium* (subclade of NrdE without aromatic interfacial residues). From these predictions (Figure S36), we find that only enzyme species from clades with aromatic interfacial residues (NrdAh and one subclade of NrdE) are predicted to have the same TrxA interaction as that observed in our cryo-EM data for the *B. subtilis* enzyme. This suggests that the observed TrxA binding mode is only present in a subset of class I RNRs, and that alternative interaction mechanisms for TrxA or other redox proteins are likely involved for other RNR species.

The class I clade from the all-RNR phylogenetic tree published previously (*2*) was pruned and used for the above analysis. Full sequences corresponding to those in the tree were retrieved from UNIPROT (*43*) and aligned with MAFFT (*69*). The sequence alignment around the TrxA binding interface was inspected and manually adjusted to improve alignment of those residues, which was then used for further analyses to identify sequences with hydrophobic interfacial residues.

AlphaFold Predictions

All AlphaFold predictions were performed in AlphaFold2 version 2.3 using the full sequence database to generate the multiple sequence alignments and a max template date of 2023-03-22.

References

1. B. L. Greene, G. Kang, C. Cui, M. Bennati, D. G. Nocera, C. L. Drennan, J. Stubbe, Ribonucleotide Reductases: Structure, Chemistry, and Metabolism Suggest New Therapeutic Targets. *Annu. Rev. Biochem.* **89**, 45–75 (2020).

2. A. A. Burnim, M. A. Spence, D. Xu, C. J. Jackson, N. Ando, Comprehensive phylogenetic analysis of the ribonucleotide reductase family reveals an ancestral clade. *Elife* **11** (2022).

3. A. A. Burnim, D. Xu, M. A. Spence, C. J. Jackson, N. Ando, Analysis of insertions and extensions in the functional evolution of the ribonucleotide reductase family. *Protein Sci.* **31**, e4483 (2022).

4. S. Licht, G. J. Gerfen, J. Stubbe, Thiyl radicals in ribonucleotide reductases. *Science* **271**, 477–481 (1996).

5. T. B. Ruskoski, A. K. Boal, The periodic table of ribonucleotide reductases. *J. Biol. Chem.* **297**, 101137 (2021).

6. J. A. Cotruvo, J. Stubbe, Class I ribonucleotide reductases: metallocofactor assembly and repair in vitro and in vivo. *Annu. Rev. Biochem.* **80**, 733–767 (2011).

7. K. Ravichandran, L. Olshansky, D. G. Nocera, J. Stubbe, Subunit Interaction Dynamics of Class Ia Ribonucleotide Reductases: In Search of a Robust Assay. *Biochemistry* **59**, 1442–1453 (2020).

8. G. Kang, A. T. Taguchi, J. Stubbe, C. L. Drennan, Structure of a trapped radical transfer pathway within a ribonucleotide reductase holocomplex. *Science* **368**, 424–427 (2020).

9. K. Yokoyama, A. A. Smith, B. Corzilius, R. G. Griffin, J. Stubbe, Equilibration of tyrosyl radicals (Y356•, Y731•, Y730•) in the radical propagation pathway of the Escherichia coli class Ia ribonucleotide reductase. *J. Am. Chem. Soc.* **133**, 18420–18432 (2011).

10. Q. Lin, M. J. Parker, A. T. Taguchi, K. Ravichandran, A. Kim, G. Kang, J. Shao, C. L. Drennan, J. Stubbe, Glutamate 52-β at the α/β subunit interface of Escherichia coli class Ia ribonucleotide reductase is essential for conformational gating of radical transfer. *J. Biol. Chem.* **292**, 9229–9239 (2017).

11. K. R. Ravichandran, E. C. Minnihan, Y. Wei, D. G. Nocera, J. Stubbe, Reverse Electron Transfer Completes the Catalytic Cycle in a 2,3,5-Trifluorotyrosine-Substituted Ribonucleotide Reductase. *J. Am. Chem. Soc.* **137**, 14387–14395 (2015).

12. M. R. Seyedsayamdost, C. T. Y. Chan, V. Mugnaini, J. Stubbe, M. Bennati, PELDOR spectroscopy with DOPA-beta2 and NH2Y-alpha2s: distance measurements between residues involved in the radical propagation pathway of E. coli ribonucleotide reductase. *J. Am. Chem. Soc.* **129**, 15748–15749 (2007).

13. H. K. Erickson, Kinetics in the pre-steady state of the formation of cystines in ribonucleoside diphosphate reductase: evidence for an asymmetric complex. *Biochemistry* **40**, 9631–9637 (2001).

14. M. Bennati, J. H. Robblee, V. Mugnaini, J. Stubbe, J. H. Freed, P. Borbat, EPR distance measurements support a model for long-range radical initiation in E. coli ribonucleotide reductase. *J. Am. Chem. Soc.* **127**, 15014–15015 (2005).

15. M. Uppsten, M. Färnegårdh, V. Domkin, U. Uhlin, The first holocomplex structure of ribonucleotide reductase gives new insight into its mechanism of action. *J. Mol. Biol.* **359**, 365–377 (2006).

16. M. R. Seyedsayamdost, J. Stubbe, Forward and reverse electron transfer with the Y356DOPA-beta2 heterodimer of E. coli ribonucleotide reductase. *J. Am. Chem. Soc.* **129**, 2226–2227 (2007).

17. M. R. Seyedsayamdost, J. Stubbe, Site-specific replacement of Y356 with 3,4-dihydroxyphenylalanine in the beta2 subunit of E. coli ribonucleotide reductase. *J. Am. Chem. Soc.* **128**, 2522–2523 (2006).

18. W. C. Thomas, F. P. Brooks 3rd, A. A. Burnim, J.-P. Bacik, J. Stubbe, J. T. Kaelber, J. Z. Chen, N. Ando, Convergent allostery in ribonucleotide reductase. *Nat. Commun.* **10**, 2653 (2019).

19. A. K. Boal, J. A. Cotruvo Jr, J. Stubbe, A. C. Rosenzweig, The dimanganese(II) site of Bacillus subtilis class Ib ribonucleotide reductase. *Biochemistry* **51**, 3861–3871 (2012).

20. M. J. Parker, X. Zhu, J. Stubbe, Bacillus subtilis class Ib ribonucleotide reductase: high activity and dynamic subunit interactions. *Biochemistry* **53**, 766–776 (2014).

21. A. Q. Hassan, Y. Wang, L. Plate, J. Stubbe, Methodology to probe subunit interactions in ribonucleotide reductases. *Biochemistry* **47**, 13046–13055 (2008).

22. E. D. Zhong, T. Bepler, B. Berger, J. H. Davis, CryoDRGN: reconstruction of heterogeneous cryo-EM structures using neural networks. *Nat. Methods* **18**, 176–185 (2021).

23. J. Sun, L. F. Kinman, D. Jahagirdar, J. Ortega, J. H. Davis, KsgA facilitates ribosomal small subunit maturation by proofreading a key structural lesion. *Nat. Struct. Mol. Biol.* **30**, 1468–1480 (2023).

24. A. Narayan, B. Berger, H. Cho, Assessing single-cell transcriptomic variability through density-preserving data visualization. *Nat. Biotechnol.* **39**, 765–774 (2021).

25. J. Ge, G. Yu, M. A. Ator, J. Stubbe, Pre-steady-state and steady-state kinetic analysis of E. coli class I ribonucleotide reductase. *Biochemistry* **42**, 10071–10083 (2003).

26. J. Jumper, R. Evans, A. Pritzel, T. Green, M. Figurnov, O. Ronneberger, K. Tunyasuvunakool, R. Bates, A. Žídek, A. Potapenko, A. Bridgland, C. Meyer, S. A. A. Kohl, A. J. Ballard, A. Cowie, B. Romera-Paredes, S. Nikolov, R. Jain, J. Adler, T. Back, S. Petersen, D. Reiman, E. Clancy, M. Zielinski, M. Steinegger, M. Pacholska, T. Berghammer, S. Bodenstein, D. Silver, O. Vinyals, A. W. Senior, K. Kavukcuoglu, P. Kohli, D. Hassabis, Highly accurate protein structure prediction with AlphaFold. *Nature* **596**, 583–589 (2021).

27. W. S. Tang, D. Silva-Sánchez, J. Giraldo-Barreto, B. Carpenter, S. M. Hanson, A. H. Barnett, E. H. Thiede, P. Cossio, Ensemble Reweighting Using Cryo-EM Particle Images. *J. Phys. Chem. B* **127**, 5410–5421 (2023).

28. M. J. Parker, "Discovery and investigation of the novel overall activity allosteric regulation of the Bacillus subtilis class Ib ribonucleotide reductase," thesis, Massachusetts Institute of Technology (2017).

29. M. J. Parker, A. O. Maggiolo, W. C. Thomas, A. Kim, S. P. Meisburger, N. Ando, A. K. Boal, J. Stubbe, An endogenous dAMP ligand in *Bacillus subtilis* class Ib RNR promotes assembly of a noncanonical dimer for regulation by dATP. *Proc. Natl. Acad. Sci. U. S. A.* **115**, E4594–E4603 (2018).

30. D. N. Mastronarde, Automated electron microscope tomography using robust prediction of specimen movements. *J. Struct. Biol.* **152**, 36–51 (2005).

31. L. V. Bock, H. Grubmüller, Effects of cryo-EM cooling on structural ensembles. *Nat. Commun.* **13**, 1709 (2022).

32. A. Punjani, J. L. Rubinstein, D. J. Fleet, M. A. Brubaker, cryoSPARC: algorithms for rapid unsupervised cryo-EM structure determination. *Nat. Methods* **14**, 290–296 (2017).

33. D. Kimanius, L. Dong, G. Sharov, T. Nakane, S. H. W. Scheres, New tools for automated cryo-EM single-particle analysis in RELION-4.0. *Biochem. J* **478**, 4169–4185 (2021).

34. T. Bepler, A. Morin, M. Rapp, J. Brasch, L. Shapiro, A. J. Noble, B. Berger, Positive-unlabeled convolutional neural networks for particle picking in cryo-electron micrographs. *Nat. Methods* **16**, 1153–1160 (2019).

35. D. Asarnow, E. Palovcak, Y. Cheng, *Asarnow/Pyem: UCSF Pyem v0.5* (2019; https://zenodo.org/record/3576630).

36. A. Punjani, H. Zhang, D. J. Fleet, Non-uniform refinement: adaptive regularization improves single-particle cryo-EM reconstruction. *Nat. Methods* **17**, 1214–1221 (2020).

37. E. C. Meng, T. D. Goddard, E. F. Pettersen, G. S. Couch, Z. J. Pearson, J. H. Morris, T. E. Ferrin, UCSF ChimeraX: Tools for structure building and analysis. *Protein Sci.* **32**, e4792 (2023).

38. R. Sanchez-Garcia, J. Gomez-Blanco, A. Cuervo, J. M. Carazo, C. O. S. Sorzano, J. Vargas, DeepEMhancer: a deep learning solution for cryo-EM volume post-processing. *Commun Biol* **4**, 874 (2021).

39. P. Virtanen, R. Gommers, T. E. Oliphant, M. Haberland, T. Reddy, D. Cournapeau, E. Burovski, P. Peterson, W. Weckesser, J. Bright, S. J. van der Walt, M. Brett, J. Wilson, K. J. Millman, N. Mayorov, A. R. J. Nelson, E. Jones, R. Kern, E. Larson, C. J. Carey, İ. Polat, Y. Feng, E. W. Moore, J. VanderPlas, D. Laxalde, J. Perktold, R. Cimrman, I. Henriksen, E. A. Quintero, C. R. Harris, A. M. Archibald, A. H. Ribeiro, F. Pedregosa, P. van Mulbregt, SciPy 1.0 Contributors, SciPy 1.0: fundamental algorithms for scientific computing in Python. *Nat. Methods* **17**, 261–272 (2020).

40. D. W. Scott, *Multivariate Density Estimation: Theory, Practice, and Visualization* (John Wiley & Sons, 2015).

41. P. V. Afonine, B. K. Poon, R. J. Read, O. V. Sobolev, T. C. Terwilliger, A. Urzhumtsev, P. D. Adams, Real-space refinement in PHENIX for cryo-EM and crystallography. *Acta Crystallogr D Struct Biol* **74**, 531–544 (2018).

42. D. Liebschner, P. V. Afonine, M. L. Baker, G. Bunkóczi, V. B. Chen, T. I. Croll, B. Hintze, L. W. Hung, S. Jain, A. J. McCoy, N. W. Moriarty, R. D. Oeffner, B. K. Poon, M. G. Prisant, R. J. Read, J. S. Richardson, D. C. Richardson, M. D. Sammito, O. V. Sobolev, D. H. Stockwell, T. C. Terwilliger, A. G. Urzhumtsev, L. L. Videau, C. J. Williams, P. D. Adams, Macromolecular structure determination using X-rays, neutrons and electrons: recent developments in Phenix. *Acta Crystallogr D Struct Biol* **75**, 861–877 (2019).

43. A. Bateman, M. Martin, S. Orchard, M. Magrane, S. Ahmad, E. Alpi, E. Bowler-Barnett, R. Britto, H. Bye-A-Jee, A. Cukura, P. Denny, T. Dogan, T. Ebenezer, J. Fan, P. Garmiri, L. J. da Costa Gonzales, E. Hatton-Ellis, A. Hussein, A. Ignatchenko, G. Insana, R. Ishtiaq, V. Joshi, D. Jyothi, S. Kandasaamy, A. Lock, A. Luciani, M. Lugarić, J. Luo, Y. Lussi, A. MacDougall, F. Madeira, M. Mahmoudy, A. Mishra, K. Moulang, A. Nightingale, S. Pundir, G. Qi, S. Raj, P. Raposo, D. L. Rice, R. Saidi, R.

Santos, E. Speretta, J. Stephenson, P. Totoo, E. Turner, N. Tyagi, P. Vasudev, K. Warner, X. Watkins, R. Zaru, H. Zellner, A. Bridge, L. Aimo, G. Argoud-Puy, A. Auchincloss, K. Axelsen, P. Bansal, D. Baratin, T. M. Batista Neto, M. Blatter, J. T. Bolleman, E. Boutet, L. Breuza, B. Gil, C. Casals-Casas, K. C. Echioukh, E. Coudert, B. A. Cuche, E. de Castro, A. Estreicher, M. Famiglietti, M. Feuermann, E. Gasteiger, P. Gaudet, S. Gehant, V. Gerritsen, A. Gos, N. Gruaz, C. Hulo, N. Hyka-Nouspikel, F. Jungo, A. Kerhornou, P. le Mercier, D. Lieberherr, P. Masson, A. Morgat, V. Muthukrishnan, S. Paesano, I. Pedruzzi, S. Pilbout, L. Pourcel, S. Poux, M. Pozzato, M. Pruess, N. Redaschi, C. Rivoire, C. J. A. Sigrist, K. Sonesson, S. Sundaram, C. H. Wu, C. Arighi, L. Arminski, C. Chen, Y. Chen, H. Huang, K. Laiho, P. McGarvey, D. Natale, K. Ross, C. R. Vinayaka, Q. Wang, Y. Wang, J. Zhang, UniProt: the Universal Protein Knowledgebase in 2023. *Nucleic Acids Res.* **51**, D523–D531 (2022).

44. P. Emsley, K. Cowtan, Coot: model-building tools for molecular graphics. *Acta Crystallogr. D Biol. Crystallogr.* **60**, 2126–2132 (2004).

45. O. S. Smart, A. Sharff, J. Holstein, T. O. Womack, C. Flensburg, P. Keller, W. Paciorek, C. Vonrhein, B. G., *Grade2 Version 1.5.0* (Cambridge, United Kingdom: Global Phasing Ltd.).

46. T. I. Croll, ISOLDE: a physically realistic environment for model building into low-resolution electron-density maps. *Acta Crystallogr D Struct Biol* **74**, 519–530 (2018).

47. D. A. Case, H. M. Aktulga, K. Belfon, D. S. Cerutti, G. A. Cisneros, V. W. D. Cruzeiro, N. Forouzesh, T. J. Giese, A. W. Götz, H. Gohlke, S. Izadi, K. Kasavajhala, M. C. Kaymak, E. King, T. Kurtzman, T.-S. Lee, P. Li, J. Liu, T. Luchko, R. Luo, M. Manathunga, M. R. Machado, H. M. Nguyen, K. A. O'Hearn, A. V. Onufriev, F. Pan, S. Pantano, R. Qi, A. Rahnamoun, A. Risheh, S. Schott-Verdugo, A. Shajan, J. Swails, J. Wang, H. Wei, X. Wu, Y. Wu, S. Zhang, S. Zhao, Q. Zhu, T. E. Cheatham 3rd, D. R. Roe, A. Roitberg, C. Simmerling, D. M. York, M. C. Nagan, K. M. Merz Jr, AmberTools. *J. Chem. Inf. Model.* **63**, 6183–6191 (2023).

48. D. A. Case, H. Metin Aktulga, K. Belfon, I. Y. Ben-Shalom, J. T. Berryman, S. R. Brozell, D. S. Cerutti, T. E. Cheatham III, G. Andrés Cisneros, V. W. D. Cruzeiro, T. A. Darden, N. Forouzesh, G. Giambasu, T. Giese, M. K. Gilson, H. Gohlke, A. W. Goetz, J. Harris, S. Izadi, S. A. Izmailov, K. Kasavajhala, M. C. Kaymak, E. King, A. Kovalenko, T. Kurtzman, T. Lee, P. Li, C. Lin, J. Liu, T. Luchko, R. Luo, M. Machado, V. Man, M. Manathunga, K. M. Merz, Y. Miao, O. Mikhailovskii, G. Monard, H. Nguyen, K. A. O'Hearn, A. Onufriev, F. Pan, S. Pantano, R. Qi, A. Rahnamoun, D. R. Roe, A. Roitberg, C. Sagui, S. Schott-Verdugo, A. Shajan, J. Shen, C. L. Simmerling, N. R. Skrynnikov, J. Smith, J. Swails, R. C. Walker, J. Wang, J. Wang, H. Wei, X. Wu, Y. Xiong, Y. Xue, D. M. York, S. Zhao, Q. Zhu, P. A. Kollman, *Amber 2023* (University of California, San Francisco, 2023).

49. A. Sali, T. L. Blundell, Comparative protein modelling by satisfaction of spatial restraints. *J. Mol. Biol.* **234**, 779–815 (1993).

50. J. Wang, W. Wang, P. A. Kollman, D. A. Case, Automatic atom type and bond type perception in molecular mechanical calculations. *J. Mol. Graph. Model.* **25**, 247–260 (2006).

51. X. He, V. H. Man, W. Yang, T.-S. Lee, J. Wang, A fast and high-quality charge model for the next generation general AMBER force field. *J. Chem. Phys.* **153**, 114502 (2020).

52. C. R. Reinhardt, P. Li, G. Kang, J. Stubbe, C. L. Drennan, S. Hammes-Schiffer, Conformational Motions and Water Networks at the α/β Interface in E. coli Ribonucleotide Reductase. *J. Am. Chem. Soc.* **142**, 13768–13778 (2020).

53. K. L. Meagher, L. T. Redman, H. A. Carlson, Development of polyphosphate parameters for use with the AMBER force field. *J. Comput. Chem.* **24**, 1016–1025 (2003).

54. P. Li, K. M. Merz Jr, MCPB.py: A Python Based Metal Center Parameter Builder. *J. Chem. Inf. Model.* **56**, 599–604 (2016).

55. G. M. J. Barca, C. Bertoni, L. Carrington, D. Datta, N. De Silva, J. E. Deustua, D. G. Fedorov, J. R. Gour, A. O. Gunina, E. Guidez, T. Harville, S. Irle, J. Ivanic, K. Kowalski, S. S. Leang, H. Li, W. Li, J. J. Lutz, I. Magoulas, J. Mato, V. Mironov, H. Nakata, B. Q. Pham, P. Piecuch, D. Poole, S. R. Pruitt, A. P. Rendell, L. B. Roskop, K. Ruedenberg, T. Sattasathuchana, M. W. Schmidt, J. Shen, L. Slipchenko, M. Sosonkina, V. Sundriyal, A. Tiwari, J. L. Galvez Vallejo, B. Westheimer, M. Włoch, P. Xu, F. Zahariev, M. S. Gordon, Recent developments in the general atomic and molecular electronic structure system. *J. Chem. Phys.* **152**, 154102 (2020).

56. R. Anandakrishnan, B. Aguilar, A. V. Onufriev, H++ 3.0: automating pK prediction and the preparation of biomolecular structures for atomistic molecular modeling and simulations. *Nucleic Acids Res.* **40**, W537-41 (2012).

57. C. Tian, K. Kasavajhala, K. A. A. Belfon, L. Raguette, H. Huang, A. N. Migues, J. Bickel, Y. Wang, J. Pincay, Q. Wu, C. Simmerling, ff19SB: Amino-Acid-Specific Protein Backbone Parameters Trained against Quantum Mechanics Energy Surfaces in Solution. *J. Chem. Theory Comput.* **16**, 528–552 (2020).

58. S. Izadi, R. Anandakrishnan, A. V. Onufriev, Building Water Models: A Different Approach. *J. Phys. Chem. Lett.* **5**, 3863–3871 (2014).

59. A. Sengupta, Z. Li, L. F. Song, P. Li, K. M. Merz Jr, Parameterization of Monovalent Ions for the OPC3, OPC, TIP3P-FB, and TIP4P-FB Water Models. *J. Chem. Inf. Model.* **61**, 869–880 (2021).

60. Z. Li, L. F. Song, P. Li, K. M. Merz Jr, Systematic Parametrization of Divalent Metal Ions for the OPC3, OPC, TIP3P-FB, and TIP4P-FB Water Models. *J. Chem. Theory Comput.* **16**, 4429–4442 (2020).

61. J. Åqvist, P. Wennerström, M. Nervall, S. Bjelic, B. O. Brandsdal, Molecular dynamics simulations of water and biomolecules with a Monte Carlo constant pressure algorithm. *Chem. Phys. Lett.* **384**, 288–294 (2004).

62. J.-P. Ryckaert, G. Ciccotti, H. J. C. Berendsen, Numerical integration of the cartesian equations of motion of a system with constraints: molecular dynamics of n-alkanes. *J. Comput. Phys.* **23**, 327–341 (1977).

63. T. Darden, D. York, L. Pedersen, Particle mesh Ewald: An N·log(N) method for Ewald sums in large systems. *J. Chem. Phys.* **98**, 10089–10092 (1993).

64. R. Salomon-Ferrer, A. W. Götz, D. Poole, S. Le Grand, R. C. Walker, Routine Microsecond Molecular Dynamics Simulations with AMBER on GPUs. 2. Explicit Solvent Particle Mesh Ewald. *J. Chem. Theory Comput.* **9**, 3878–3888 (2013).

65. G. M. Torrie, J. P. Valleau, Nonphysical sampling distributions in Monte Carlo free-energy estimation: Umbrella sampling. *J. Comput. Phys.* **23**, 187–199 (1977).

66. A. Grossfield, An Implementation of WHAM: The Weighted Histogram Analysis Method, version 2.0. 9. 18. (2014).

67. D. R. Roe, T. E. Cheatham 3rd, PTRAJ and CPPTRAJ: Software for Processing and Analysis of Molecular Dynamics Trajectory Data. *J. Chem. Theory Comput.* **9**, 3084–3095 (2013).

68. M. R. Shirts, C. Klein, J. M. Swails, J. Yin, M. K. Gilson, D. L. Mobley, D. A. Case, E. D. Zhong, Lessons learned from comparing molecular dynamics engines on the SAMPL5 dataset. *J. Comput. Aided Mol. Des.* **31**, 147–161 (2017).

69. K. Katoh, J. Rozewicki, K. D. Yamada, MAFFT online service: multiple sequence alignment, interactive sequence choice and visualization. *Brief. Bioinform.* **20**, 1160–1166 (2017).